

TIFR-TH/05-12  
OUTP-0507P

# Probing the deviation from maximal mixing of atmospheric neutrinos

Sandhya Choubey<sup>\*a</sup> and Probir Roy<sup>†b</sup>

<sup>a</sup>*Rudolf Peierls Centre for Theoretical Physics, University of Oxford,  
1 Keble Road, Oxford OX1 3NP, UK*

<sup>b</sup>*Department of Theoretical Physics, Tata Institute of Fundamental Research,  
Homi Bhabha Road, Mumbai 400 005, India*

PACS numbers: 14.60.Pq, 13.15.+g, 14.60.Lm, 96.40.Tv

## Abstract

Pioneering atmospheric muon neutrino experiments have demonstrated the near-maximal magnitude of the flavor mixing angle  $\theta_{23}$ . But the precise value of the deviation  $D \equiv 1/2 - \sin^2 \theta_{23}$  from maximality (if nonzero) needs to be known, being of great interest – especially to builders of neutrino mass and mixing models. We quantitatively investigate in a three generation framework the feasibility of determining  $D$  in a statistically significant manner from studies of the atmospheric  $\nu_\mu, \bar{\nu}_\mu$  survival probability including both vacuum oscillations and matter effects. We show how this determination will be sharpened by considering the up-down ratios of observed  $\nu_\mu$ - and  $\bar{\nu}_\mu$ -induced events and the differences of these ratios in specified energy and zenith angle bins. We consider 1 Megaton year of exposure to a magnetized iron calorimeter such as the proposed INO detector ICAL, taking into account both energy and zenith angle resolution functions. The sensitivity of such an exposure and the dependence of the determination of  $D$  on the concerned oscillation parameters are discussed in detail. The vital use of matter effects in fixing the octant of  $\theta_{23}$  is highlighted.

<sup>\*</sup> email: sandhya@thphys.ox.ac.uk

<sup>†</sup> email: probir@theory.tifr.res.in

# 1 Introduction

Neutrino oscillation studies have come of age after the recent results from the Super-Kamiokande (SK) [1], K2K [2], SNO [3] and KamLAND [4] experiments. The existence of oscillations in atmospheric [5] and accelerator generated [2]  $\nu_\mu$ 's and  $\bar{\nu}_\mu$ 's with a modulus of squared mass difference<sup>1</sup>  $|\Delta m_{31}^2| \sim 2.1 \times 10^{-3} \text{ eV}^2$  ( $1.4 \times 10^{-3} \text{ eV}^2 < |\Delta m_{31}^2| < 3.3 \times 10^{-3} \text{ eV}^2$  at  $3\sigma$ ) and a mixing angle  $\theta_{23} \sim 45^\circ$  ( $35^\circ < \theta_{23} < 54^\circ$  at  $3\sigma$ ) as well as in solar [3, 6] (reactor [4])  $\nu_e$ 's ( $\bar{\nu}_e$ 's) with a squared mass difference<sup>1</sup>  $\Delta m_{21}^2 \sim 8 \times 10^{-5} \text{ eV}^2$  ( $7.4 \times 10^{-5} \text{ eV}^2 < \Delta m_{21}^2 < 9.5 \times 10^{-5} \text{ eV}^2$  at  $3\sigma$ ) and a mixing angle  $\theta_{12} \sim 34^\circ$  ( $30^\circ < \theta_{12} < 40^\circ$  at  $3\sigma$ ) is now an accepted fact [7]. The goals of the next generation of experiments include both increased precision in the already measured oscillation parameters and the determination of the still unknown quantities such as  $\theta_{13}$  (presently bounded by  $0 < \theta_{13} < 12^\circ$  at  $3\sigma$  [7, 8]) as well as the sign of  $\Delta m_{31}^2$  and eventually the CP violating phase  $\delta$  in the PMNS matrix. An issue of great importance right now is the precise value of  $\theta_{23}$  which dominantly controls  $\nu_\mu$ - $\nu_\tau$  oscillations. The presently allowed range of  $\theta_{23}$  does not enable one to distinguish it from its maximal<sup>2</sup> value  $\pi/4$ . A naturally arising question is: how can one significantly narrow down this range in the future and possibly detect a nonzero deviation

$$D \equiv \frac{1}{2} - \sin^2 \theta_{23} \quad (1)$$

from maximal mixing. This is what we consider in the context of forthcoming<sup>3</sup> studies of atmospheric  $\nu_\mu$ 's and  $\bar{\nu}_\mu$ 's.

Let us mention some current theoretical ideas regarding  $\theta_{23}$ . A simple way of understanding a maximal value for  $\theta_{23}$  is to invoke the concept of a  $\mu$ - $\tau$  exchange symmetry [10]. Though this immediately leads to  $\theta_{23} = \pi/4$ , it also yields at the same time a vanishing  $\theta_{13}$  and CP conservation in the neutrino sector. While the last two features could in principle turn out to be the facts of Nature, our current hopes are to the contrary. A nonzero and measurable  $\theta_{13}$  as well as the occurrence of CP violation in the neutrino sector can lead to much that is interestingly new in neutrino physics and can be studied in laboratory experiments with reactor, accelerator, atmospheric, solar and supernova neutrinos. The general expectation [10], therefore, is that any  $\mu$ - $\tau$  interchange symmetry, if present, must be broken so as to allow a nonvanishing  $\theta_{13}$  and (possibly observable) CP violation in the neutrino sector. Such a breaking would generally cause  $D$  to be different from zero. However, its magnitude and sign would be given by the yet undetermined symmetry breaking mechanism. Another idea has been that of quark-lepton complementarity [11]. In this approach a bimaximal neutrino Majorana mass matrix is “rotated” by a unitary matrix diagonalizing charged left chiral leptons in generation space. The latter is postulated to be the same as the CKM matrix resulting in a reduction of  $\theta_{12}$  from  $\pi/4$  by an amount comparable to the Cabibbo angle  $\theta_C \sim 13^\circ$  in conformity with observation. In this case  $\theta_{23}$  also is expected to

<sup>1</sup>We work in the conventional picture of three neutrino flavors with CPT conservation assumed. We also employ standard notation where  $m_{ij}^2 = m_i^2 - m_j^2$  and  $\theta_{ij}$  plus  $\delta$  are defined by the PMNS matrix of our Eq. (2) in §2.

<sup>2</sup>Two flavor  $\nu_\mu$ - $\bar{\nu}_\mu$  oscillations in vacuum are controlled by  $\theta_{23}$  only through the factor  $\sin^2 2\theta_{23}$  which is highest when  $\theta_{23}$  has the maximal value  $\pi/4$ . Matter effects and  $\Delta m_{21}^2$ -driven subdominant atmospheric neutrino oscillations have different dependence on  $\theta_{23}$ .

<sup>3</sup>An analysis of the allowed range of  $D$ , based on extant atmospheric  $\nu_\mu + \bar{\nu}_\mu$  data, is available in [9].

be reduced from  $45^\circ$  by an amount of the order of  $\sin^{-1} s_{23}^{\text{CKM}} \sim 2.4^\circ$  so that  $D$  is expected to be positive and in the vicinity of 0.04. However, variants [11] of this hypothesis exist with  $D$  predicted to be significantly different from 0.04. There are many other model predictions, utilizing flavor symmetries, GUT relations and textures, covering  $|D|$  from 0.005 to  $\geq 0.16$ , as listed in Table II of [12].

We thus see that an experimental measurement of  $D$  would be of great interest to the builders of neutrino mass matrix models. Apart from the magnitude of  $|D|$ ,  $\text{sgn}(D)$  is also of importance. Its determination would fix the octant of  $\theta_{23}$ , *i.e.* whether  $\theta_{23}$  exceeds or is less than  $\pi/4$ . With the goal of determining  $D$ , one can explore different experimental options. A detailed survey of the capabilities of forthcoming and futuristic accelerator based long baseline neutrino/antineutrino experiments along this line has already been given in [12, 13]. Here we want to consider future atmospheric neutrino studies guided by our knowledge of extant ones [9]. A major new venture in this direction will be the proposed Hyper-Kamiokande/UNO/MEMPHYS type of experiments [14] with Megaton water Cerenkov detectors. Detailed studies [15, 16, 17] have been made (among other things) of the  $\nu_\mu + \bar{\nu}_\mu$  survival probability, information on which will emanate from such a detector. While this kind of data can yield information also on  $D$  [9], it will be largely from the vacuum oscillations of  $\nu_\mu$  and  $\bar{\nu}_\mu$  and will be less sensitive to matter effects. Depending on the mass ordering of the neutrinos (normal or inverted), larger matter effects appear in the neutrino or antineutrino channel for long baseline distances ( $L > 1000$  km). In addition, the sign of the earth matter effect term in the difference of survival probabilities  $\Delta P_{\mu\mu}$  (as defined in §2) depends on the energy and zenith angle of the atmospheric  $\nu_\mu/\bar{\nu}_\mu$ . Since water Cerenkov atmospheric neutrino experiments measure the  $\nu_\mu + \bar{\nu}_\mu$  survival probability and since their poor detector resolution means that the data collected would have to be grouped into very broad sub-GeV and multi-GeV energy bins as in the SK data sample, matter effects in this class of experiments will be partially washed out. In order to maximize the extraction of information from the individual survival probabilities of atmospheric  $\nu_\mu$ 's and  $\bar{\nu}_\mu$ 's, propagating both through vacuum and through earth, one needs to measure them separately as a function of energy and baseline length. In fact, the individual survival probabilities will be measurable in a large magnetized iron calorimeter such as the ICAL detector of the proposed INO experiment [18]. This experiment is expected to have a good detector resolution allowing fine binning of the data in energy and zenith angle, essential for gleaning out the  $D$  dependence of earth matter effects. Our aim is to focus on the feasibility of utilizing the data in future from such a detector to determine  $D$ .

There have already been several studies [19, 20, 21] of the possibility of determining the normal or inverted nature of the mass ordering of neutrinos, *i.e.*  $\text{sgn}(\Delta m_{31}^2)$ , in magnetized iron calorimetric detectors. The question of the determination of  $D$  has been touched upon [20] but not analyzed in detail. In this paper we carry out a detailed study of the feasibility of a measurement of both the magnitude and the sign of  $D$  from data simulated for 1 Megaton year of exposure of a large magnetized iron calorimeter, such as ICAL, to atmospheric muon neutrinos and antineutrinos. In principle, a magnetized iron calorimetric detector in an underground observatory (such as the proposed INO laboratory) could also study other types of events: upward going muons and electron neutrino events. As a first step, we would like to restrict our studies to fully contained events only and hence do not consider upward going muons, which are much harder to incorporate. Furthermore, the large thickness [18] of the iron plates of the proposed

ICAL detector precludes the detection of electrons and will not trigger on to events induced by  $\nu_e$ s and  $\bar{\nu}_e$ s. This is why we confine ourselves to atmospheric  $\nu_\mu, \bar{\nu}_\mu$  studies. Furthermore, ICAL is designed to have a detection threshold of neutrino energy = 1 GeV and therefore cannot study sub-GeV events. This is why we consider the multi-GeV regime only. We take a three generation system and use exact numerical solutions of the neutrino (and antineutrino) equations of motion in the atmosphere and in earth matter using the PREM [22] density profile as an input. We assume what we regard as reasonable energy and zenith angle resolution functions for the detector and concentrate on up-down asymmetry ratios [20]  $U_N/D_N$  and  $U_A/D_A$  for  $\nu_\mu$ - and  $\bar{\nu}_\mu$ -induced events in appropriate energy and zenith angle bins. We are then able to pinpoint the precise bins from where the utilizable information on *both* vacuum oscillations and matter effects can be extracted – leading to a determination of  $D$ . We also show how the use of matter effects through the difference  $U_N/D_N - U_A/D_A$  will enable one to fix the sign of  $D$  and resolve the octant ambiguity in  $\theta_{23}$ .

The paper is organized in the following way. Section 2 contains a slightly simplified and approximate analytical treatment of the survival probabilities of  $\nu_\mu$ 's and  $\bar{\nu}_\mu$ 's propagating in matter of constant density; this is to bring out the basic physics issues in question, specifically, highlighting the phenomenon of resonance. In §3 we present our numerical results on the  $\nu_\mu$  survival probability (after propagation in earth matter) as it varies with the energy  $E$  and baseline length  $L$ ; in particular, the occurrence of extrema in this variation is highlighted through the definitions of SPMIN1, SPMAX and SPMIN2 which appear. Section 4 comprises the methodology for the extraction of the up-down asymmetry ratios  $U_N/D_N$  and  $U_A/D_A$  from the simulated data. The details of our statistical ( $\chi^2$ ) analysis are presented in §5. The determination of  $|D|$  from the simulated data and the estimated intervals on both sides of  $D = 0$  for which this will be possible at the  $3\sigma$  level are given in §6. The procedure for the fixation of the sign of  $D$  (and hence the octant of  $\theta_{23}$ ) is described in §7. In §8, which contains our summary and conclusions, we also provide a discussion of the sensitivity of an ICAL-like detector to  $D$ , as compared to the forthcoming long baseline and water Cerenkov detector studies with accelerator generated and atmospheric neutrinos respectively.

## 2 Approximate analytical treatment of $\nu_\mu/\bar{\nu}_\mu$ survival probability in matter

In the standard parametrization, the Pontecorvo-Maki-Nakagawa-Sakata [23] matrix is given by

$$U = \begin{pmatrix} c_{12}c_{13} & s_{12}c_{13} & s_{13}e^{-i\delta} \\ -s_{12}c_{23} - c_{12}s_{23}s_{13}e^{i\delta} & c_{12}c_{23} - s_{12}s_{23}s_{13}e^{i\delta} & s_{23}c_{13} \\ s_{12}s_{23} - c_{12}c_{23}s_{13}e^{i\delta} & c_{12}s_{23} - s_{12}s_{23}s_{13}e^{i\delta} & c_{23}c_{13} \end{pmatrix}. \quad (2)$$

In Eq. (2)  $c_{ij} = \cos \theta_{ij}$ ,  $s_{ij} = \sin \theta_{ij}$  and, while the phase  $\delta$  has been retained, the two Majorana phases have been ignored since they do not contribute to neutrino oscillations. The effective Hamiltonian for such oscillations in matter with varying density can be expressed in the flavor

basis as a function of the path length  $x$  of the neutrino from its source. Thus

$$H(x) = \frac{1}{2E} U \begin{pmatrix} 0 & 0 & 0 \\ 0 & \Delta m_{21}^2 & 0 \\ 0 & 0 & \Delta m_{31}^2 \end{pmatrix} U^\dagger + \begin{pmatrix} V(x) & 0 & 0 \\ 0 & 0 & 0 \\ 0 & 0 & 0 \end{pmatrix}. \quad (3)$$

In Eq. (3),  $\Delta m_{ij}^2 \equiv m_i^2 - m_j^2$ ,  $m_i$  and  $E$  being the mass of the  $i$ th (physical) neutrino and the neutrino energy respectively, whereas the potential  $V(x)$  is given by

$$V(x) = \sqrt{2} G_F N_e(x). \quad (4)$$

Here  $N_e(x)$  is the electron density of matter, so that the potential can be rewritten as

$$V(x) = (7.56 \times 10^{-14}) \frac{\rho(x)}{\text{gms/cc}} Y_e(x) \text{ eV}, \quad (5)$$

$\rho(x)$  being the density of earth matter in the path of the neutrino and  $Y_e(x)$  ( $\simeq 0.5$ ) being the number of electrons per nucleon in the same.

The neutrino evolution operator  $S(x, 0)$  has the matrix element

$$S_{\gamma\beta}(x, 0) = \langle \nu_\gamma(x) | \nu_\beta(0) \rangle, \quad (6)$$

$\beta, \gamma$  being flavor indices. This obeys the evolution Equation

$$i \frac{dS_{\gamma\beta}(x, 0)}{dx} = [H(x), S(x, 0)]_{\gamma\beta}. \quad (7)$$

The probability for a neutrino flavor transition  $\beta \rightarrow \gamma$  at a baseline length  $L$  is given by

$$P_{\beta\gamma}(L) \equiv P[\nu_\beta(0) \rightarrow \nu_\gamma(L)] = |S_{\gamma\beta}(L, 0)|^2. \quad (8)$$

In case the earth matter density  $\rho$  is taken<sup>4</sup> to be constant between the production and detection points of the neutrino, the potential  $V$  also becomes a constant. It is then useful to diagonalize the Hamiltonian of Eq. (3) with eigenvalues  $\lambda_{1,2,3}(2E)^{-1}$ .

$$H = \frac{1}{2E} U^M \begin{pmatrix} \lambda_1 & 0 & 0 \\ 0 & \lambda_2 & 0 \\ 0 & 0 & \lambda_3 \end{pmatrix} U^{M\dagger}, \quad (9)$$

$U^M$  being the lepton mixing matrix in matter. Then one can write

$$S_{\gamma\beta}(L, 0) = \sum_{i=1}^3 U_{\gamma i}^{M*} e^{-i\lambda_i L(2E)^{-1}} U_{\beta i}^M, \quad (10)$$

$$\begin{aligned} P_{\beta\gamma}(L) = & \delta_{\beta\gamma} - 4 \sum_{j>1} \Re \left( U_{\beta i}^M U_{\gamma i}^{M*} U_{\beta j}^{M*} U_{\gamma j}^M \right) \sin^2 \frac{\Delta m_{ij}^2 L}{4E} \\ & + 2 \sum_{j>1} \Im \left( U_{\beta i}^M U_{\gamma i}^{M*} U_{\beta j}^{M*} U_{\gamma j}^M \right) \sin \frac{\Delta m_{ij}^2 L}{2E}. \end{aligned} \quad (11)$$

$E$ in GeV	$L$ in km	$A$	$A\Delta$
1	1000	0.099	0.252
	3000	0.125	0.953
	5000	0.131	1.673
	7000	0.155	2.754
	9000	0.171	3.908
	11000	0.229	6.409
3	1000	0.297	0.252
	3000	0.375	0.953
	5000	0.395	1.673
	7000	0.465	2.754
	9000	0.513	3.908
	11000	0.688	6.409
5	1000	0.495	0.252
	3000	0.626	0.953
	5000	0.659	1.673
	7000	0.775	2.754
	9000	0.855	3.908
	11000	1.147	6.409
7	1000	0.693	0.252
	3000	0.876	0.953
	5000	0.922	1.673
	7000	1.084	2.754
	9000	1.197	3.908
	11000	1.606	6.409
9	1000	0.892	0.252
	3000	1.126	0.953
	5000	1.185	1.673
	7000	1.394	2.754
	9000	1.538	3.908
	11000	2.064	6.409

Table 1: Variation of  $\Delta$  and  $A\Delta$  with  $E$  and  $L$  assuming  $\rho$  to be constant and equal to 4.52 gms/cc.

More specifically, the muon neutrino and antineutrino survival probabilities are given by

$$P_{\mu\mu}(L) = 1 - 4 \left( |U_{\mu 1}^M|^2 |U_{\mu 2}^M|^2 \sin^2 \frac{\lambda_1 - \lambda_2}{4E} L + |U_{\mu 1}^M|^2 |U_{\mu 3}^M|^2 \sin^2 \frac{\lambda_1 - \lambda_3}{4E} L + |U_{\mu 2}^M|^2 |U_{\mu 3}^M|^2 \sin^2 \frac{\lambda_2 - \lambda_3}{4E} L \right), \quad (12)$$

$$P_{\bar{\mu}\bar{\mu}}(L) = P_{\mu\mu}(L, V \rightarrow -V). \quad (13)$$

The elements of  $U^M$ , appearing in Eqs. (9), can be parametrized in the same way as the ‘vacuum’ mixing matrix  $U$  of Eq. (2) except that one needs to use the corresponding values of the angles and the phase in matter, i.e.  $\theta_{ij} \rightarrow \theta_{ij}^M$  and  $\delta \rightarrow \delta^M$ .

Tractable analytic expressions  $P_{\alpha\beta}(L)$  emerge only after some additional approximations. For the purpose of displaying the relevant analytic expressions, in addition to assuming the constancy<sup>4</sup> of  $\rho$  and hence of  $V$ , we choose to neglect  $\mathcal{O}(s_{13}^3)$  and  $\mathcal{O}(\alpha^2)$  terms,  $\alpha$  being  $\Delta m_{21}^2/\Delta m_{31}^2$ . From what was discussed in §1, we already know that

$$s_{13}^3 < 0.008, \quad (14)$$

$$\alpha^2 \simeq 0.001. \quad (15)$$

Therefore these approximations do not generally make any significant practical difference from the exact numerical results, as will be seen later. On the other hand, they do enable us to display the two quantities of our interest, namely  $P_{\mu\mu}^{vac}$ , which is the muon neutrino survival probability in vacuum, and  $\Delta P_{\mu\mu}(L) \equiv P_{\mu\mu}(L) - P_{\bar{\mu}\bar{\mu}}(L)$ , which is the difference between the muon neutrino and antineutrino survival probabilities in matter, in analytic form, making their physical features rather transparent. The eigenvalues of  $\lambda_{1,2,3}$  and the elements of the matrix  $U^M$  of Eq. (9) can be calculated within the above mentioned approximations following the method described in Ref. [24]. They can then be substituted in Eq. (11) to compute  $P_{\mu\mu}^{vac}(L)$  and  $\Delta P_{\mu\mu}(L)$  for atmospheric neutrinos.

In order to display the desired analytic expressions, we first define a dimensionless quantity

$$\Delta \equiv \frac{\Delta m_{31}^2 L}{4E}. \quad (16)$$

The expression for  $P_{\mu\mu}^{vac}$  can now be given as [24]

$$P_{\mu\mu}^{vac} = 1 - 4s_{23}^2 c_{23}^2 (1 - c_{13}^2 s_{23}^2) \sin^2 \Delta + 4\alpha c_{12} c_{23} (c_{12} c_{23} - 2s_{13} s_{12} s_{23}^3 \cos \delta) \Delta \sin 2\Delta + \mathcal{O}(\alpha^2, s_{13}^3). \quad (17)$$

---

<sup>4</sup>This is an inaccurate assumption for the passage of GeV and multi-GeV atmospheric neutrinos through the earth when  $L$  exceeds 1000 km. However, we need this assumption only for displaying analytic expressions. Our numerical results are obtained without assuming a constant  $\rho$ , and actually, with the PREM [22] earth matter density profile as an input. Moreover, they are correct to all orders in  $\alpha \equiv \Delta m_{21}^2/\Delta m_{31}^2$  and  $s_{13}$ .

For the description of matter effects, it is convenient to define another dimensionless quantity

$$A \equiv \frac{2EV}{\Delta m_{31}^2}. \quad (18)$$

For atmospheric muon neutrinos of GeV and multi-GeV energies and low to large pathlengths, the magnitude of  $A$  varies from about 0.1 to about 2.1. On the other hand, the energy independent  $A\Delta$  varies from about 0.25 to about 6.4 for  $\rho \simeq 4.52$  gm/cc, cf. Table 1, where the values of these parameters have been given for various choices of  $E$  and  $L$ . The expression for  $\Delta P_{\mu\mu}(L)$  now reads [24]

$$\begin{aligned} \Delta P_{\mu\mu}(L) = & 4s_{13}^2 s_{23}^2 \left[ \frac{\sin^2(1+A)\Delta}{(1+A)^2} - \frac{\sin^2(1-A)\Delta}{(1-A)^2} \right] \\ & - 8s_{13}^2 c_{23}^2 s_{23}^2 \left[ \sin \Delta \cos A \Delta \left\{ \frac{\sin(1+A)\Delta}{(1+A)^2} - \frac{\sin(1-A)\Delta}{(1-A)^2} \right\} + \Delta \sin 2\Delta \frac{A}{1-A^2} \right] \\ & - 8\alpha s_{13} c_{12} s_{12} c_{23} s_{23} \cos \delta \left[ \cos \Delta \frac{\sin A \Delta}{A} \left\{ \frac{\sin(1+A)\Delta}{1+A} - \frac{\sin(1-A)\Delta}{1-A} \right\} \right. \\ & \left. + (c_{23}^2 - s_{23}^2) \sin \Delta \left\{ \sin \Delta \frac{2A}{1-A^2} + \frac{\sin A \Delta}{A} \left( \frac{\cos(1+A)\Delta}{1+A} - \frac{\cos(1-A)\Delta}{1-A} \right) \right\} \right] \\ & + O(\alpha^2, s_{13}^3). \end{aligned} \quad (19)$$

This expression vanishes for  $s_{13} = 0$ , clearly showing the need for the latter to have a nonzero value in order to make  $\Delta P_{\mu\mu}$  nonzero. If the limit  $\alpha \rightarrow 0$  is taken and the “small  $A$ ” approximation is used<sup>5</sup>, retaining only linear terms in  $A$ , Eq. (19) reduces to

$$\Delta P_{\mu\mu} \simeq -16A(1/2 - |U_{\mu 3}|^2)|U_{e 3}|^2|U_{\mu 3}|^2(\Delta \sin 2\Delta - 2 \sin^2 \Delta) \quad (20)$$

in agreement with the result first reported in Ref. [25]. In this approximate limit, though not in general,  $\Delta P_{\mu\mu}^A$  is directly proportional to  $|U_{e 3}|^2(1/2 - |U_{\mu 3}|^2)$ . The more general dependence on  $s_{13}$  and  $D$  is, of course, hidden in Eq. (19).

The last-mentioned  $\alpha \rightarrow 0$  limit may in fact be more relevant than being a mere device to get to Eq. (20). Given (1) the accidental feature that the atmospheric  $\nu_\mu/\nu_e$  ratio would have been  $\sim 2$  in the relevant energy range if  $\nu_\mu \rightleftharpoons \nu_\tau$  oscillations were absent and (2) the fact of a near-maximal  $\theta_{23}$ , the effect of the solar neutrino squared mass difference  $\Delta m_{21}^2$  on atmospheric neutrino oscillations can be shown to be small [26]. It may therefore be useful to display also the analytical expression for the survival probabilities of muon neutrinos and antineutrinos with the assumptions of only the constancy of  $\rho$  and the neglect of  $\mathcal{O}(\alpha)$  terms. Taking the limit  $\alpha \rightarrow 0$  and using the notation of Eqs. (16) and (18), one then has

$$\lim_{\alpha \rightarrow 0} \lambda_1 = \frac{1}{2} \left[ \Delta m_{31}^2 (A + 1) - (\Delta m_{31}^2)^M \right],$$

---

<sup>5</sup>From Table 1, the linear  $A$  approximation would appear to be accurate to within 90% only for neutrino energies below 3 GeV and pathlengths below 9000 km.

$$\begin{aligned}\lim_{\alpha \rightarrow 0} \lambda_2 &= 0, \\ \lim_{\alpha \rightarrow 0} \lambda_3 &= \frac{1}{2} [\Delta m_{31}^2 (A + 1) + (\Delta m_{31}^2)^M],\end{aligned}\quad (21)$$

for neutrinos with

$$(\Delta m_{31}^2)^M = \Delta m_{31}^2 |(A - 1)| \left[ 1 + 4s_{13}^2 (A - 1)^{-2} \right]^{1/2} \quad (22)$$

and replacing  $A$  by  $-A$  for antineutrinos. Furthermore, it follows that

$$\lim_{\alpha \rightarrow 0} |U_{\mu 1}^M| = |s_{23} s_{13}^M|, \quad (23)$$

$$\lim_{\alpha \rightarrow 0} |U_{\mu 2}^M| = |c_{23}|, \quad (24)$$

$$\lim_{\alpha \rightarrow 0} |U_{\mu 3}^M| = |s_{12} c_{13}^M|, \quad (25)$$

where  $s_{13}^M \equiv \sin \theta_{13}^M$ ,  $c_{13}^M = \cos \theta_{13}^M$  and  $\theta_{13}^M$  is given in terms of  $\theta_{13}$  and  $A$  by the relation

$$\sin^2 2\theta_{13}^M = \sin^2 2\theta_{13} \left( \frac{\Delta m_{31}^2}{(\Delta m_{31}^2)^M} \right)^2 = \frac{\sin^2 2\theta_{13}}{(A - \cos 2\theta_{13})^2 + \sin^2 2\theta_{13}}. \quad (26)$$

Eqs. (20) – (25) enable us to rewrite Eqs. (12) and (13) in the limit  $\alpha \rightarrow 0$  as

$$\lim_{\alpha \rightarrow 0} P_{\mu\mu}(L) = 1 - P_{\mu\mu}^1(L) - P_{\mu\mu}^2(L) - P_{\mu\mu}^3(L), \quad (27)$$

$$P_{\bar{\mu}\bar{\mu}}(L) = P_{\mu\mu}(L, A \rightarrow -A), \quad (28)$$

with

$$P_{\mu\mu}^1(L) = \sin^2 \theta_{13}^M \sin^2 2\theta_{23} \sin^2 \frac{\Delta m_{31}^2 (A + 1) - (\Delta m_{31}^2)^M}{8E} L, \quad (29)$$

$$P_{\mu\mu}^2(L) = \cos^2 \theta_{13}^M \sin^2 2\theta_{23} \sin^2 \frac{\Delta m_{31}^2 (A + 1) + (\Delta m_{31}^2)^M}{8E} L, \quad (30)$$

$$P_{\mu\mu}^3(L) = \sin^2 2\theta_{13}^M \sin^4 \theta_{23} \sin^2 \frac{(\Delta m_{31}^2)^M}{4E} L. \quad (31)$$

We note that  $P_{\mu\mu}^1(L)$  vanishes in vacuum (when matter effects go to zero), but  $P_{\mu\mu}^{2,3}$  do not. In §3, we shall numerically study the behavior of  $P_{\mu\mu}^{1,2,3}(L)$  as functions of the neutrino energy  $E$  for different baseline lengths  $L$ . The expression for  $\sin^2 2\theta_{13}^M$  in Eq. (26) shows the effect of the MSW resonance when  $A$  equals  $\cos 2\theta_{13}$ , i.e.

$$E = E_{\text{res.}} \equiv \frac{\Delta m_{31}^2 \cos 2\theta_{13}}{2\sqrt{2}G_F N_e}. \quad (32)$$

Though  $E_{\text{res.}}$  of Eq. (32) has no explicit dependence on  $L$ , in practice an implicit  $L$  dependence creeps in through  $N_e$  for path lengths involving significant spatial variations of the earth's density. Furthermore, at or near the resonance, Eq. (19) would not be trustworthy since, with  $s_{13}$  small,  $A$  is rather close to unity – making some of the RHS terms blow up. At  $E = E_{\text{res.}}$ ,  $\sin^2 2\theta_{13}^M$  reaches its maximum value, i.e. unity. For  $\Delta m_{31}^2 = (2 - 3) \times 10^{-3} \text{ eV}^2$  and a small  $\theta_{13}$ , the resonance could occur [27] for atmospheric muon neutrinos passing through the earth with energies between 5 and 10 GeV. At resonance, the conversion probability of a muon neutrino becomes sizable even for a small  $\theta_{13}$ . The effect of a small nonzero  $\theta_{13}$  could then be observed as an excess of upward going electron neutrinos.

### 3 Numerical results on $\nu_\mu$ survival probability in matter

We now present our results for the muon neutrino survival probability  $P_{\mu\mu}$  in vacuum and in matter. To obtain these, we have numerically solved the three-generation differential equation of motion of the neutrinos exactly, using the PREM profile for the earth matter densities [22]. Fig. 1 shows  $P_{\mu\mu}$  as a function of  $L$ , for six different fixed values of  $E$ . This plot (as well as subsequent plots presented in this paper except where specified otherwise) has been generated with chosen benchmark values of the other concerned oscillation parameters  $\Delta m_{31}^2$ ,  $\Delta m_{21}^2$ ,  $\sin^2 \theta_{12}$ ,  $\sin^2 \theta_{13}$  and  $\delta$  – as tabulated in Table 2 – and two values of  $\sin^2 \theta_{23}$  as explained in the caption. The following features are evident from Fig. 1.

$\Delta m_{31}^2 = 2 \times 10^{-3} \text{ eV}^2$
$\Delta m_{21}^2 = 8 \times 10^{-5} \text{ eV}^2$
$\sin^2 \theta_{12} = 0.28$
$\sin^2 2\theta_{13} = 0.1$
$\delta = 0$

Table 2: Chosen benchmark values of oscillation parameters, except  $\theta_{23}$ , with assumed normal mass ordering.

- Matter effects inside the mantle begin to be significant for  $E \gtrsim 4 \text{ GeV}$ ,  $L \gtrsim 4000 \text{ km}$  and are largest for  $E$  between 5 and 6 GeV, reducing a bit for  $E = 7 \text{ GeV}$ .
- For  $E \gtrsim 4 \text{ GeV}$  and inside the mantle, the survival probability in matter at the peaks invariably reduces from its value of near unity in vacuum. This effect increases as  $\sin^2 \theta_{23}$  is increased from 0.36 to 0.5 and beyond.

- For  $E \gtrsim 4$  GeV and inside the mantle, matter effects tend to increase the survival probability at the troughs from its vacuum value of  $P_{\mu\mu} = 1 - 4c_{13}^2 c_{23}^2 (1 - c_{13}^2 c_{23}^2)$ . This increase however reduces as the value of  $\sin^2 \theta_{23}$  is raised from 0.36 to 0.5 and beyond.
- For  $E \gtrsim 4$  GeV and  $L$  large but within the mantle (specifically between 8000 km and 10000 km), the matter contribution to the survival probability, i.e.  $P_{\mu\mu} - P_{\mu\mu}^{vac}$ , can change sign.
- The survival probability in matter has a fairly sharp discontinuity at the mantle-core boundary and behaves very differently with distance inside the core as compared with the mantle.

For a given neutrino energy  $E$ , matter effects begin to be significant only when the neutrinos pass through matter densities which are close to their resonant value. Lower energy neutrinos need higher matter densities to hit the resonance condition and vice versa, as can be seen from Eq. (32). Since, for upward going atmospheric neutrinos, the average density of the earth increases as  $L$  increases,  $E_{res}(av)$  of Eq. (32) decreases with  $L$ . In Fig. 2 we show the resonance energy  $E_{res}(av)$ , calculated from Eq. (32) with the benchmark (Table 2) values of  $\sin^2 2\theta_{13}$  and  $\Delta m_{31}^2$ , as a function of the distance  $L$  travelled by an atmospheric  $\nu_\mu$  inside the earth. For each  $L$ , the average earth matter density has been calculated using the PREM density profile. For  $L < 1000$  km, the resonance energy  $E_{res}$  clearly exceeds 9 GeV. Since the flux of multi-GeV atmospheric neutrinos falls very fast [28] with energy and since we restrict our analysis to fully contained neutrino events in the detector with  $E < 11$  GeV, we do not expect much matter effect for these short baselines.

In order to understand the extent of matter effects for  $L > 1000$  km, we need to take into account another factor apart from the difference between  $E$  and  $E_{res}$ . That is the role of the  $\Delta m_{31}^2$ -dependent oscillatory terms in Eq. (27). In this context, it is instructive to start by looking at the extrema of the oscillatory term  $\sin^2(1.27\Delta m_{31}^2 L/E)$ , where  $\Delta m_{31}^2$  is in  $eV^2$ ,  $L$  is in km and  $E$  in GeV. We define  $E_{SPMIN1}$ ,  $E_{SPMAX}$  and  $E_{SPMIN2}$  as the respective values of the energy corresponding to the first<sup>6</sup> minimum, the first maximum and the second minimum in the survival probability  $P_{\mu\mu}$  as  $L/E$  increases. In other words, these respectively correspond to the first maximum, the first minimum and the second maximum as  $L/E$  increases in the flavor conversion probability  $\sum_{\beta=e,\tau} P_{\mu\beta}$ . Their values in vacuum are,

$$E_{SPMIN1} = \frac{2}{\pi}(1.27)\Delta m_{31}^2 L, \quad (33)$$

$$E_{SPMAX} = \frac{1}{\pi}(1.27)\Delta m_{31}^2 L, \quad (34)$$

$$E_{SPMIN2} = \frac{2}{3\pi}(1.27)\Delta m_{31}^2 L, \quad (35)$$

are plotted, along with  $E_{res}$ , against  $L$  in Fig. 2. We deduce from this figure that  $E_{res} \simeq E_{SPMIN1}$  for  $L \simeq 4500$  km, while  $E_{res} \simeq E_{SPMAX}$  for  $L \simeq 7400$  km and  $E_{res} \simeq E_{SPMIN2}$  for  $L \simeq 9700$  km.

---

<sup>6</sup>This means first or second (as the case may be) starting from the *left* in Fig. 1, but first or second starting from the *right* in Figs. 3 and 4.

Concentrating on the region  $1000 \text{ km} < L < 4000 \text{ km}$ , we find that here  $7.4 \text{ GeV} < E_{res} < 9.6 \text{ GeV}$ , and  $E_{res} \gg E_{SPMIN1}$  so that once again the survival probability  $P_{\mu\mu}$  is not much affected by earth matter. In contrast, for  $L > 4000 \text{ km}$  and with  $E$  between 5 and 7 GeV, large matter effects ensue, as evident from Fig. 1.

The three terms  $P_{\mu\mu}^1$ ,  $P_{\mu\mu}^2$  and  $P_{\mu\mu}^3$ , as defined in Eq. (27) and given analytically in Eqs. (29)–(31), are shown in Fig. 3 as functions of the neutrino energy  $E$  for the three special baseline lengths mentioned above:  $L = 4500 \text{ km}$  (upper panels),  $7000 \text{ km}$  (middle panels) and  $9700 \text{ km}$  (lower panels). The dotted blue lines in Fig. 3 show these three terms in vacuum for  $\sin^2 \theta_{23} = 1/2$ , while the other lines show them in the presence of matter for different values of  $\sin^2 \theta_{23}$ , as explained in the caption. For these plots we have taken  $\Delta m_{21}^2 = 0$ , while the other parameters are as in Fig. 1. We discuss below the behavior of the three terms  $P_{\mu\mu}^{1,2,3}$  separately<sup>7</sup>.

1.  $P_{\mu\mu}^1$  is proportional to  $\sin^2 \theta_{13}^M$ , cf. Eq. (29). Though, approximately equal to  $\sin^2 \theta_{13}$  for  $E \ll E_{res}$ ,  $\sin^2 \theta_{13}^M$  increases with  $E$  and reaches the value 1/2 at  $E = E_{res}$ . Beyond  $E_{res}$ ,  $\sin^2 \theta_{13}^M$  continues to rise with  $E$  till it saturates to the maximum value of unity for  $E \gg E_{res}$ . For  $L = 4500 \text{ km}$ , one has  $S_- \equiv \sin^2[\{\Delta m_{31}^2(A+1) - (\Delta m_{31}^2)^M\}L/8E] \sim 1$  for most part of the energy range in Fig. 3. However, for  $L = 7000 \text{ km}$ ,  $S_-$  is  $\sim 0.2$  in magnitude at  $E = 1 \text{ GeV}$  and rises monotonically to  $\sim 0.9$  at  $E = 9 \text{ GeV}$ . As a result, for both baseline lengths of  $4500 \text{ km}$  and  $7000 \text{ km}$ ,  $P_{\mu\mu}^1$  increases monotonically with energy. For  $L = 9700 \text{ km}$ ,  $S_-$  is  $\sim 0.8$  around  $E = 1 \text{ GeV}$ , but falls to almost zero at  $E = 7 \text{ GeV}$  and rises yet again to  $\sim 0.3$  at  $E = 9 \text{ GeV}$ . The consequence is that  $P_{\mu\mu}^1$ , which is a product of a continuously rising  $\sin^2 \theta_{13}^M$  and the oscillatory  $S_-$  factor, has a complicated behavior as a function of energy at  $L = 9700 \text{ km}$ . We recall here that  $P_{\mu\mu}^1 = \Delta P_{\mu\mu}^1 \equiv P_{\mu\mu}^1 - P_{\mu\mu}^{1,vac}$  is a pure matter effect term and hence always positive.
2. The second term  $P_{\mu\mu}^2$  is the dominant term in vacuum. For  $E \ll E_{res}$ , there is very little matter effect in it and  $P_{\mu\mu}^2$  remains close to its vacuum value. As  $E$  increases towards  $E_{res}$  and beyond,  $\cos^2 \theta_{13}^M$ , which appears as a factor in  $P_{\mu\mu}^2$ , decreases towards 0.5 at  $E_{res}$  and eventually to near-zero for  $E \gg E_{res}$ . For  $E < E_{res}$  and all values of  $L$ , the matter-dependent oscillatory factor  $S_+ \equiv \sin^2[\{\Delta m_{31}^2(A+1) + (\Delta m_{31}^2)^M\}L/8E]$  closely follows the behavior of the corresponding  $\sin^2(\Delta m_{31}^2 L/4E)$  term in vacuum. But the situation changes drastically for  $E > E_{res}$ . Now the said  $S_+$  factor is almost unity at  $L = 4500 \text{ km}$  and  $9700 \text{ km}$ , but nearly vanishes at  $L = 7000 \text{ km}$ . Thus we can describe all the cases for  $P_{\mu\mu}^2$  in the following way. While  $P_{\mu\mu}^2$  follows its vacuum oscillation pattern for  $E < E_{res}$ , it falls to almost zero as  $E$  increases beyond  $E_{res}$ . The latter behavior ensues at  $L = 4500 \text{ km}$  and  $9700 \text{ km}$  due to the fall of  $\cos^2 \theta_{13}^M$  to zero, whereas at  $L = 7000 \text{ km}$  it is caused by  $S_+$  nearly vanishing. For  $E \sim E_{res}$ ,  $\Delta P_{\mu\mu}^2 \equiv P_{\mu\mu}^2 - P_{\mu\mu}^{2,vac}$  is positive at  $L = 7000 \text{ km}$  but negative at  $L = 4500$  and  $9700 \text{ km}$ .
3. Turning to  $P_{\mu\mu}^3$ , we see from Eq. (31) that its proportionality to  $\sin^2 2\theta_{13}^M \sin^2[(\Delta m_{31}^2)^M L/4E]$  makes it very small in vacuum owing to the smallness of  $\sin^2 2\theta_{13}$ . In matter, however, the growth of  $\sin^2 2\theta_{13}^M$  with energy (for  $E \lesssim E_{res}$ ) till its maximum value at  $E = E_{res}$  makes

<sup>7</sup>For a similar discussion on the dependence of matter effects in  $P_{\mu\mu}$  on  $L$  and  $E$  see [21].

$P_{\mu\mu}^3$  increase appreciably in this energy range. For our example cases shown in Fig. 3, ( $E \simeq 5$  GeV and maximal  $\theta_{23}$ ), it increases from about 0.01, 0.0 and 0.025 in vacuum at  $L = 4500, 7000$  and  $9700$  km respectively to about 0.14, 0.20 and 0.25 in earth matter. This means that, at  $E \sim E_{res}$ ,  $\Delta P_{\mu\mu}^3 \equiv P_{\mu\mu}^3 - P_{\mu\mu}^{3,vac}$  is in general positive for all  $L$ .

The impact of earth matter effects is largest for any  $L$  at  $E = E_{res}$  when the sum of the three terms  $P_{\mu\mu}^1$ ,  $P_{\mu\mu}^2$  and  $P_{\mu\mu}^3$  becomes most different from its value in vacuum. In fact,  $P_{\mu\mu}^{1,vac}$  ( $P_{\mu\mu}^{3,vac}$ ) is exactly (nearly) zero for all  $E$ , while – for  $E \sim 5 - 7$  GeV –  $P_{\mu\mu}^{2,vac}$  yields SPMIN1 at  $L = 4500$  km, SPMAX at  $L = 7000$  km and SPMIN2 at  $L = 9700$  km. While matter effects raise  $P_{\mu\mu}^{1,3}$  for all  $L$  and  $E$  (cf. Fig. 3), apart from mildly increasing  $P_{\mu\mu}^2$  at SPMAX for  $L = 7000$  km, they decrease it when  $L = 4500$  (SPMIN2) and  $9700$  km (SPMIN2). There is thus an important difference between the SPMAX and the two SPMIN cases: matter effects come with the same relative sign for all the three terms at SPMAX, but increase  $P_{\mu\mu}^{1,3}$  and decrease  $P_{\mu\mu}^2$  at SPMIN1 and SPMIN2. The SPMAX case at  $L = 7000$  km thus exhibits the largest effects of earth matter in the total survival probability  $P_{\mu\mu}$  for  $E \sim 5 - 7$  GeV. In contrast, these effects partially cancel in the two SPMIN cases between the increase in  $P_{\mu\mu}^{1,3}$  and the decrease in  $P_{\mu\mu}^2$ . For  $L = 4500$  km (SPMIN1), this cancellation is particularly important and the total  $P_{\mu\mu}$  has very little residual matter effect. Therefore we shall ignore SPMIN1 in our subsequent matter effect discussion. For  $L = 9700$  km (SPMIN2), the cancellation is not complete and appreciable matter effects do persist in  $P_{\mu\mu}$ . As noted earlier, one characteristic of the SPMAX case ( $L = 7000$  km and  $E \sim 5$  GeV) is the decrease in  $P_{\mu\mu}$  from its maximal value of near-unity in the presence of matter since all the three terms  $P_{\mu\mu}^{1,2,3}$  increase. In contrast,  $P_{\mu\mu}$  increases on account of matter in the SPMIN2 case ( $L = 9700$  km,  $E \sim 5$  GeV, as exemplified here) because of the dominant decrease in  $P_{\mu\mu}^2$ .

We can comment on the respective roles of  $\theta_{13}$  and  $\theta_{23}$  in determining the effects of matter on the muon neutrino survival probability. First, the value of  $\theta_{13}$ , of course, directly controls the extent of such effects. Figs. 1 – 3 have been generated with  $\sin^2 2\theta_{13} = 0.1$ . For the same  $L$  (and hence the same average matter density), the value of  $E_{res}$  is larger for a smaller  $\theta_{13}$ , cf. Eq. (32). On the other hand, the value of  $(\Delta m_{31}^2)^M$  is smaller in that case for a constant matter density independent of  $L$ . The result is a larger mismatch between  $E_{res}$  (at which  $\sin^2 2\theta_{13}^M$  becomes maximal) and the energy where  $P_{\mu\mu}^{2,3}$  reach their extremal values. Matter effects in  $P_{\mu\mu}$  are therefore reduced for a smaller  $\theta_{13}$ . Second, Fig. 1 carries evidence of the dependence of the contribution of matter effects to  $P_{\mu\mu}$  on  $\sin^2 \theta_{23}$ . The nature and extent of this dependence is more clearly brought out by Eqs. (29–31) and Fig. 3. While  $P_{\mu\mu}^{1,2}$  are seen to be proportional to  $\sin^2 2\theta_{23}$ , the third term  $P_{\mu\mu}^3$  goes as  $\sin^4 \theta_{23}$ . A noteworthy point in this connection is that, when  $\theta_{23}$  is close to being maximal, any change in its value affects  $\sin^2 2\theta_{23}$  much less than  $\sin^2 \theta_{23}$ . For instance, when  $\theta_{23}$  decreases from  $45^\circ$  to  $40^\circ$ ,  $\sin^2 2\theta_{23}$  changes from 1 to 0.97, i.e. by 3%, while  $\sin^2 \theta_{23}$  is reduced by 16% from 0.5 to 0.41. This is reflected in essentially no visible change in  $P_{\mu\mu}^{1,2}$  when  $\sin^2 \theta_{23}$  is reduced<sup>8</sup> (increased) from 0.5 to 0.4 (0.6), cf. Fig. 1. On the other hand,  $P_{\mu\mu}^3$  does increase appreciably as  $\sin^2 \theta_{23}$  is increased from 0.4 to 0.5 leading to an increased  $\theta_{23}$  sensitivity in a muon neutrino disappearance experiment on account of matter effects. As noted earlier, the net decrease (increase) of the total  $\nu_\mu$  survival probability  $P_{\mu\mu}$  due to matter effects at SPMAX (SPMIN2) increases (decreases) as the value of  $\sin^2 \theta_{23}$  is increased. This behavior can

<sup>8</sup> $\sin^2 2\theta_{23}$  is the same for  $\sin^2 \theta_{23} = 0.4$  or 0.6.

now be understood from the dependence of  $P_{\mu\mu}^3$  on  $\sin^2 \theta_{23}$ . Let us first consider SPMAX. Since the increase due to matter effects in  $P_{\mu\mu}^3$  causes a decrease in the total survival probability  $P_{\mu\mu}$  at SPMAX and since  $P_{\mu\mu}^3$  in matter increases as  $\sin^2 \theta_{23}$  increases, the matter-induced decrease of  $P_{\mu\mu}$  at SPMAX increases with increasing  $\sin^2 \theta_{23}$ . For the SPMIN2 case, the dependence of  $P_{\mu\mu}^3$  on  $\sin^2 \theta_{23}$ , as discussed above, is more subtle. In reality, the main role of the increase in  $P_{\mu\mu}^3$  due to matter is to wash out the corresponding decrease in  $P_{\mu\mu}^2$ . Therefore, the matter-induced relative increase of the survival probability  $P_{\mu\mu}$  at SPMIN2 decreases as  $\sin^2 \theta_{23}$  increases.

It is pertinent to stress a couple of points here. First, the strong dependence on  $\sin^2 \theta_{23}$  of the total survival probability  $P_{\mu\mu}$  in matter coming from  $P_{\mu\mu}^3$ , as discussed above, implies that observed atmospheric  $\nu_\mu, \bar{\nu}_\mu$  events could be used not only to probe  $|D| \equiv |1/2 - \sin^2 \theta_{23}|$  but also the sign of  $D$  to determine if  $\theta_{23} < \pi/4$  or  $> \pi/4$ , thus resolving the ambiguity regarding the octant of  $\theta_{23}$ . The second issue is the effect of earth matter on the shape of the survival probability as a function of the neutrino energy. This is shown in Fig. 4 for six different choices for  $L$ . The various choices of  $\sin^2 \theta_{23}$  are given in the figure caption while the other parameters are the same as in Fig. 1. This figure again tells us that matter effects lower (raise)  $P_{\mu\mu}$  from its vacuum values at SPMAX (SPMIN1 and SPMIN2), resulting in a relative change of the shape of  $P_{\mu\mu}$  as a function of  $E$ . These matter-dependent effects will of course be projected onto the observed atmospheric muon neutrino spectrum which will come folded with  $P_{\mu\mu}$ . A detector with good energy resolution should be sensitive to the spectral shape of atmospheric muon neutrinos and hence should pick out the shape distortion owing to matter effects.

## 4 Up-down asymmetry in an ICAL-like detector

A very powerful variable, which clearly displays oscillation effects for atmospheric neutrinos (antineutrinos), is the up-down ratio [29]  $U_N/D_N$  ( $U_A/D_A$ ). Here  $U_N$  ( $U_A$ ) is the number of events recorded for the “upward” muon neutrinos (antineutrinos) coming with  $\cos \xi < 0$  and  $D_N$  ( $D_A$ ) is the number of atmospheric events recorded for the “downward” muon neutrinos (antineutrinos) with  $\cos \xi > 0$ ,  $\xi$  denoting the zenith angle of the  $\nu_\mu/\bar{\nu}_\mu$  trajectory. Downward (upward) neutrinos and antineutrinos cover short (long) distances. Hence downward ones hardly undergo any flavor transformation while upward ones are subjected to full flavor oscillations, the relevant oscillation lengths being in the range  $10^2 - 10^3$  km. Thus the up-down ratio  $U/D$  yields crucial information on the degree of oscillations for upward neutrinos and antineutrinos. Being relatively insensitive<sup>9</sup> to the uncertainties in the atmospheric neutrino flux calculations, it is a reliable measure of the survival probability  $P_{\mu\mu}$ . As such, it can be used to study both the vacuum oscillations of muon neutrinos and the effect of matter on them [20]. We shall consider the above ratio for atmospheric muon neutrino and antineutrino events in a large magnetized iron calorimetric detector. Such a detector named ICAL, has been conceived in the proposed underground neutrino laboratory INO [18] in India. While the initial proposal is for a detector mass of 50 kton for ICAL, the aim is to enlarge it to a final detector size of 100 kton. The proposed detector would have a modular structure with stacks of  $\sim 6$  cm thick magnetized iron plates interleaved with  $\sim 2.5$  cm of resistive plate chambers (RPC) made of glass as the active detector material. A uniform magnetized field

---

<sup>9</sup>We have more to say on this issue later in this section.

of  $1 - 1.4$  Tesla would enable the charge discrimination of muons distinguishing between  $\nu_\mu$ - and  $\bar{\nu}_\mu$ -induced events. The full detector would be divided into three modules, the modular structure allowing the start of detector operations with those modules that are ready even when others are still under construction. Further details are given in [18].

The expected number of  $\mu$  (or  $\bar{\mu}$ ) events, induced by oscillating atmospheric muon neutrinos (or antineutrinos) and recorded in a detector such as ICAL, is given by

$$N_l = n_T \int_{\xi_{min}}^{\xi_{max}} d \cos \xi \int_0^\pi d \xi' \tilde{R}(\xi, \xi') \int_{E_{min}}^{E_{max}} dE \int_0^\infty dE' \tilde{R}(E, E') \sigma_l(E') \epsilon_l(E') \\ \times \left[ \frac{d^2 \phi_l(E', \xi')}{dE' d \cos \xi'} P_{ll}(E', \xi') + \frac{d^2 \phi_{l'}(E', \xi')}{dE' d \cos \xi'} P_{l'l}(E', \xi') \right], \quad (36)$$

where,  $E'$  and  $E$  are the true and experimentally reconstructed neutrino energies respectively and  $\tilde{R}(E, E')$  is the energy resolution function of the detector. Likewise,  $\xi'$  and  $\xi$  are the true and reconstructed neutrino zenith angle and  $R(\xi, \xi')$  is the zenith angle resolution function of the detector. It is convenient for us to adopt<sup>10</sup> Gaussian forms for the energy and length (zenith angle) resolution functions of the detector:

$$\tilde{R}(x, x') = \frac{1}{\sqrt{2\pi}\sigma_{x'}} \exp\left(\frac{-(x - x')^2}{2\sigma_{x'}^2}\right), \quad (37)$$

where  $x$  is  $E$  or  $\xi$  ( $L$ ). For the energy resolution we assume  $2\sigma_{E'} = 0.3E'$ . The detector resolution for the zenith angle and hence the distance travelled by the neutrino is expected to be somewhat better and we assume  $2\sigma_{L'} = 0.2L'$ . These numbers are more or less the same as the full widths of the nonGaussian resolution functions given in [18]. The total distance  $L$  and the zenith angle  $\xi$  are related by

$$L = \sqrt{(R_e + h)^2 - R_e^2 \sin^2 \xi} - R_e \cos \xi, \quad (38)$$

where  $R_e$  is the radius of the earth and  $h$  the height of the atmosphere. Among the rest of the quantities of Eq. (36),  $n_T$  denotes the number of target nucleons times the total live time of the detector,  $\sigma_l(E')$  is the total  $\nu_l N \rightarrow lX$  scattering cross-section of a  $\nu_l$  of energy  $E'$  and  $\epsilon_l(E')$  is the trigger efficiency of the magnetized calorimeter. Here the index  $l$  can be  $\mu$  or  $\bar{\mu}$  and  $d^2 \phi_l/dE' d \cos \xi'$  is the differential flux of atmospheric neutrinos  $\nu_l$ . Finally,  $P_{ll}$  gives the survival probability for the atmospheric  $\nu_\mu$  (or  $\bar{\nu}_\mu$ ) and  $P_{l'l}$  the transition probability of  $\nu'_l$  to  $\nu_l$ ,  $l'$  being either  $e$  or  $\bar{e}$  correlated to  $l$  being  $\mu$  or  $\bar{\mu}$ .

We shall present our results for a 100 kT of active detector mass and ten years of running, assuming a conservative 50% trigger efficiency<sup>11</sup> for the detector<sup>12</sup>. In order to calculate the number of detected events, we use the latest three-dimensional atmospheric neutrino fluxes provided by Honda *et. al.* [28], which is also used by the INO collaboration [18]. For the reaction cross-section

<sup>10</sup>We have checked that for the  $E$  and  $L$  bin sizes used in this paper the resolution functions make only little difference to the final results. Hence, the precise form of the resolution function is unimportant.

<sup>11</sup>In reality, this could be as high as 80%, S. R. Dugad, private communication.

<sup>12</sup>For any other detector mass and efficiency, the statistics can be accordingly scaled.

we consider only the DIS process and use the cross-sections given by the CTEQ collaboration [30]. We then distribute the number of  $\mu^-$  ( $\mu^+$ ) events induced by the  $\nu_\mu$  ( $\bar{\nu}_\mu$ ), into various zenith angle and energy bins. In the range  $E = 1 - 11$  GeV, the events are divided into five energy bins, each of width 2 GeV. The zenith angle binning is presented in Table 3. The bins 1–6 (7–12) correspond to  $\cos \xi > 0$  ( $< 0$ ) and hence contain downward (upward) going neutrinos/antineutrinos. Upward going ones have been binned according to  $L_m$ , the distance they travel within earth matter. The range of  $L_m$  (in km), corresponding to each zenith angle bin, is given in Table 3. The bins for downward neutrinos are arranged to have a structure similar to that of upward neutrinos. We simulate the “data” for the prototype detector, assuming certain “true” values for the oscillation parameters namely those benchmarked in Table 2, and distribute them into the five energy bins and the twelve zenith angle bins. Thus we have  $5 \times 12 = 60$  bins of data for the muon events. The iron detector we consider is magnetized and therefore has charge discrimination capability. So we have 60 bins of  $\mu^-$  data for the neutrino channel and another 60 bins of  $\mu^+$  data for the antineutrino channel. Our total data set therefore comprises 120 bins.

The up-down ratio  $U_N/D_N$  for  $\nu_\mu$ ’s is shown in five different energy bins in Fig. 5. However, instead of integrating over all upward and downward zenith angles, we have chosen to divide the said ratio into six zenith angle bins. Each of the panels in Fig. 5 contains  $U_N/D_N$  for a certain range of the modulus of the zenith angle as shown in the legend. For instance, the first (last) panel on the top left (bottom right) contains the ratio  $U_N/D_N$  for  $0 \leq |\cos \xi| \leq 0.157$  ( $0.785 \leq |\cos \xi| \leq 1$ ) and calculated by taking upward going neutrinos with  $-0.157 \leq \cos \xi \leq 0$  ( $-1 \leq \cos \xi \leq -0.785$ ) and downward going neutrinos with  $0 \leq \cos \xi \leq 0.157$  ( $0.785 \leq \cos \xi \leq 1$ ). The black and magenta solid lines in Fig. 5 describe the  $U_N/D_N$  spectrum for the realistic case of upward neutrinos travelling through earth matter and with  $\sin^2 \theta_{23} = 0.5$  and  $\sin^2 \theta_{23} = 0.36$  respectively. In contrast, the similar dashed lines show the hypothetical  $U_N/D_N$  spectrum for the corresponding values of  $\sin^2 \theta_{23}$ , if the upward neutrinos were assumed to be travelling in vacuum even inside the earth. For the same value of  $\sin^2 \theta_{23}$ , a comparison of the solid line with the corresponding dashed line shows the effect of earth matter in changing the muon neutrino up-down ratio. Furthermore, the degree of this change is seen to depend on the value of  $\sin^2 \theta_{23}$ .

An even better way of bringing out matter effects<sup>13</sup> in atmospheric muon neutrinos is to look at the difference  $U_N/D_N - U_A/D_A$ , where the subscript  $A$  now refers to  $\bar{\nu}_\mu$ ’s. The up-down ratio  $U/D$  yields  $P_{\mu\mu}$  which is the same for neutrinos and antineutrinos in vacuum so long as CPT is conserved. Therefore, the difference in the up-down ratio between neutrinos and antineutrinos gives a direct measure of the matter effects in  $P_{\mu\mu}$ . In fact, it relates to  $\Delta P_{\mu\mu}$  of Eq. (19). Fig. 6 shows our results for the same choice of zenith angle and energy bins and for the same set of oscillation parameters with an assumed normal mass ordering as made in Fig. 5. Substantial matter effects in terms of the deviation of the difference  $U_N/D_N - U_A/D_A$  from zero are concretely shown in Fig. 6 and in a more pronounced manner in the right hand panels. Once again, the strength of the matter part in the survival probability is seen to depend on the value of  $\sin^2 \theta_{23}$ .

We can summarize the main characteristic features of Figs. 5 and 6 as follows:

---

<sup>13</sup>For a normal (inverted) mass ordering, matter effects at baseline lengths  $L > 1000$  km for  $\nu_\mu$ ’s ( $\bar{\nu}_\mu$ ’s) are significantly larger than for  $\bar{\nu}_\mu$ ’s ( $\nu_\mu$ ’s), cf. discussion at the end of the section.

- For a normal mass ordering ( $\Delta m_{31}^2 > 0$ ), atmospheric muon neutrinos undergo significant matter effects for  $E \gtrsim 3$  GeV and  $L \gtrsim 4000$  km. A similar statement holds true for muon antineutrinos if  $\Delta m_{31}^2 < 0$ .
- Matter effects increase (decrease) the ratio  $U_N/D_N$  in the  $E$  and  $\cos \xi$  bins corresponding to the SPMINs (SPMAX) for a normal mass ordering. For an inverted mass ordering, a similar statement can be made about  $U_A/D_A$ .
- The largest impact of earth matter comes in the bin  $E = 5 - 7$  GeV and  $-0.628 \leq \cos \xi \leq -0.471$  ( $6000 \leq L_m \leq 8000$  km), corresponding to the SPMAX. Here  $U_N/D_N - U_A/D_A$  reduces for a normal mass ordering to  $-0.3$  to  $-0.25$ , depending on the value of  $\sin^2 \theta_{23}$ .
- The dependence of the strength of matter effects on the value of  $\sin^2 \theta_{23}$  is most clearly brought out in the energy and zenith angle bin mentioned in the preceding bullet. Reducing  $\sin^2 \theta_{23}$  from the maximal 0.5 to 0.36 brings a nearly 10% change in the difference  $U_N/D_N - U_A/D_A$ . This highlights the possible role of matter effects in achieving a better sensitivity to  $\sin^2 \theta_{23}$  and hence a better resolution of its difference from maximality.

Let us make two further comments. First, the main advantage of the up-down asymmetry parameter, constructed from directly recorded events, is its insensitivity to the error in the absolute normalization of the atmospheric neutrino flux, on account of cancellations between the upward and downward fluxes. Recall that this uncertainty has been the main source of systematic error in extracting the mass squared difference and mixing parameters from any set of observed atmospheric neutrino events. Additionally, the charge discrimination capability of an ICAL type of a detector should be able to bring out earth matter effects in the atmospheric neutrino signal much more effectively by constructing the difference  $U_N/D_N - U_A/D_A$  from recorded events. The second comment relates to our assumption of a normal neutrino mass ordering, automatically implying larger matter effects in the  $\nu_\mu$  rather than the  $\bar{\nu}_\mu$  channel for  $L > 1000$  km. In case Nature has chosen an inverted ordering of the neutrino masses, the above features would hold qualitatively except that the situation would be reversed between the  $\nu_\mu$  and  $\bar{\nu}_\mu$ . In particular, the major change in the plot of Fig. 6 would be that of a sign.

## 5 Details of the Statistical Analysis

Our twin goal is to check the sensitivity of atmospheric  $\nu_\mu$ 's and  $\bar{\nu}_\mu$ 's to any deviation of  $\theta_{23}$  from its maximal value  $\pi/4$  and to see the effects of earth matter on this sensitivity. In order to achieve this end, we perform a statistical analysis of simulated “data” generated in an ICAL-like calorimeter, assuming certain “true” values for the oscillation parameters. For our error analysis we define a  $\chi^2$  parameter following [31, 32, 33] as

$$\chi_{atm}^2 \equiv \min_{\xi_k} \left[ \sum_{n=1}^{120} \left( \frac{\tilde{N}_n^{theory} - N_n^{data}}{\sigma_n^{stat}} \right)^2 + \sum_{k=1}^K \xi_k^2 \right] , \quad (39)$$

bin	$\cos \xi$	Total distance $L$ in km	Distance in earth $L_m$ in km
1	1.000 to 0.785	15.0 – 19.1	0
2	0.785 to 0.628	19.1 – 23.8	0
3	0.628 to 0.471	23.8 – 31.7	0
4	0.471 to 0.314	31.7 – 47.3	0
5	0.314 to 0.157	47.3 – 91.5	0
6	0.157 to 0.000	91.5 – 437.4	0
7	0.000 to -0.157	437.4 – 2091.5	0 – 2000
8	-0.157 to -0.314	2091.5 – 4047.3	2000 – 4000
9	-0.314 to -0.471	4047.3 – 6031.7	4000 – 6000
10	-0.471 to -0.628	6031.7 – 8023.8	6000 – 8000
11	-0.628 to -0.785	8023.8 – 10019.1	8000 – 10000
12	-0.785 to -1.000	10019.1 – 12757.0	10000 – 12500

Table 3: The zenith angles bins used.

In Eq. (39)  $N_n^{data}$  are the observed number of events in bin  $n$  and  $\sigma_n^{stat}$  are the statistical errors. The systematic errors in the data and the theory are accounted for through the set of pulls  $\{\xi_k\}$ . The latter are defined in such a way that the number of expected events  $N_n^{theory}$ , in bin  $n$ , corresponds to  $\xi_k = 0$  and their  $1\sigma$  deviations are given by  $\xi_k = \pm 1$ . The theoretical and experimental uncertainties then cause the expected number of events to shift to  $\tilde{N}_n^{theory}$ :

$$\tilde{N}_n^{theory} = N_n^{theory} \left[ 1 + \sum_{k=1}^K \pi_n^k \xi_k \right] + \mathcal{O}(\xi_k^2) , \quad (40)$$

In Eq. (40)  $\tilde{N}_n^{theory}$  has been expanded in powers of  $\xi_k$ , keeping only linear terms. The quantities  $\pi_n^k$  give the fractional rate of change of  $N_n^{theory}$  due to the  $k$ th systematic uncertainty.

The most important theoretical systematic uncertainties come from our lack of knowledge of the predicted atmospheric neutrino fluxes. In order to cover these, we take an absolute normalization error of 20%, a “tilt” factor of 5% to account for the spectral uncertainty, an uncertainty of 5% in the neutrino-antineutrino flux ratio and an uncertainty of 5% in the zenith angle dependence. For the DIS cross-sections, we consider an uncertainty of 10% – assuming a modest improvement in our present understanding of these cross-sections by the time ICAL starts operating. For the other experimental systematic uncertainties, we take a 5% consolidated error. We take these somewhat arbitrarily assumed plausible systematic errors for the proposed experiment, pending actual estimates to be provided by the INO collaboration in future. We calculate the uncertainties  $\pi_n^k$  in Eq. (40) using an approach similar to that used in [31]. Therefore,  $\pi_n^k$  is taken as 20%, 10% and 5% of the number of events for all bins when  $k$  corresponds to the absolute flux normalisation, cross-section uncertainty and experimental systematic error respectively. The  $\pi_n^k$ s for  $k$  corresponding to the “tilt” factor and zenith angle dependence of the  $\nu_\mu$  and  $\bar{\nu}_\mu$  flux are calculated using the method detailed in [31]. For the flux uncertainty coming from neutrino-antineutrino flux ratio, we take  $\pi_n^k = 2.5\%$  of the number of events for all the neutrino bins and  $\pi_n^k = -2.5\%$  of number of events for all the antineutrino bins.

Unless otherwise stated, for the numerical analysis done in this paper, the number of “data” events  $N_n^{data}$  in the  $n$ th bin is simulated at “true” values<sup>14</sup> of the parameter set  $\{p \text{ (true)}\}$ ,  $p$  covering  $\Delta m_{31}^2$ ,  $\Delta m_{21}^2$ ,  $\sin^2 \theta_{12}$  and  $\delta$ , which are set at the corresponding benchmark values listed in Table 2. The choice of a normal mass ordering is for the sake of being definite rather than on account of any theoretical prejudice. We shall also present some results for the inverted mass ordering. The true values of the remaining oscillation parameters  $\sin^2 \theta_{23}$  and  $\sin^2 \theta_{13}$  will be varied to account for their impact on matter effects and will be stated explicitly as and when used. (Any change, whenever made in the assumed true values of the other parameters, will also be mentioned explicitly.) For each such simulated data set, we do a statistical analysis using Eqs. (39) and (40) to find the sensitivity of ICAL to any deviation of  $\theta_{23}$  from maximality as well as to the fixation of its right octant.  $\tilde{N}_n^{theory}$  is calculated for a given set of oscillation parameters using Eq. (40). The RHS of Eq. (39) is then minimized with respect to the pulls  $\xi_k$  to obtain  $\chi_{atm}^2$  as a function of the oscillation parameters. The latter function is then further minimized by varying the oscillation parameters within their allowed ranges to obtain the sensitivity plots for  $\theta_{23}$ .

The extent of earth matter effects is determined by the true value of  $\sin^2 \theta_{13}$ . Therefore, we also include the constraints on  $\sin^2 \theta_{13}$  expected to ensue from the combined data expected from the next generation reactor [34] and long baseline accelerator [35] experiments. So we define the *combined*  $\chi^2$  for the ICAL experiment as

$$\chi_{comb}^2 = \chi_{atm}^2 + \left( \frac{\sin^2 \theta_{13} - \sin^2 \theta_{13}(\text{true})}{\sigma_{s_{13}^2}} \right)^2. \quad (41)$$

In Eq. (41),  $\chi_{atm}^2$  is as given by Eq. (39). Furthermore, the second RHS term tries to take into account the above-mentioned bounds on  $\sin^2 \theta_{13}$  from future laboratory experiments with the denominator  $\sigma_{s_{13}^2}$  denoting the  $1\sigma$  uncertainty in it which is assumed [36] to be at the level of 3.5%.

## 6 Deviation of $\theta_{23}$ from its maximal value

Let us turn now to the focal point of this paper: how well will the deviation of  $\theta_{23}$ , if any, from its maximal value be probed with atmospheric neutrinos in the foreseeable future? We take the combined information from 1 MtonY of simulated data in ICAL, adding on the constraint on  $\sin^2 \theta_{13}$  to come from future reactor and accelerator experiments. Our procedure is to generate the data at a certain nonmaximal value of  $\sin^2 \theta_{23}(\text{true})$  and then fit this data with the maximal muon neutrino mixing angle  $\theta_{23} = \pi/4$ , choosing different values of  $\sin^2 \theta_{23}(\text{true})$ . The results are displayed in Fig. 7. At each point in this  $\Delta m_{31}^2(\text{true}) - \sin^2 \theta_{23}(\text{true})$  plane, we simulate the 120 bin data in ICAL, taking  $\sin^2 \theta_{13}(\text{true}) = 0.00$  (left panel), 0.02 (middle panel) and 0.04 (right panel) respectively and assuming for all the other parameters the benchmark values given in Table

<sup>14</sup>In what follows, we shall always distinguish between the “true” values of the oscillation parameters chosen by Nature at which we generate our projected data and the fitted values of those parameters which are constrained by the same data. The true values will henceforth be written as  $\sin^2 \theta_{23}(\text{true})$  etc., while the fitted values will be referred to as  $\sin^2 \theta_{23}$  etc.

2 to be true. Each such data set is then fitted back using Eqs. (40), (39) and (41) with  $N_n^{theory}$  calculated for maximal  $\theta_{23}$  mixing. The parameters  $\Delta m_{31}^2$  and  $\sin^2 \theta_{13}$  are allowed to take any possible values in the fitted  $N_n^{theory}$ , while  $\Delta m_{21}^2$  and  $\sin^2 \theta_{12}$  are allowed to vary freely within 7% and 15% of their assumed true values respectively<sup>15</sup>.

The upper and lower panels of Fig. 7 correspond to respective exposures of 1 MtonY and 3.37 MtonY<sup>16</sup>. The regions of  $\sin^2 \theta_{23}(\text{true})$  and  $\Delta m_{31}^2(\text{true})$  within the white, blue and green bands of Fig. 7 show the true values of those quantities for which the distinction of a maximal from a true nonmaximal value of  $\theta_{23}$  will not be possible at the  $1\sigma$ ,  $2\sigma$  and  $3\sigma$  levels respectively for the specified exposure. The broken lines give the corresponding limits of  $\sin^2 \theta_{23}(\text{true})$  in case earth matter effects were deliberately switched off by hand. Among those the long-dashed, dot-dashed and dotted lines respectively yield the  $1\sigma$ ,  $2\sigma$  and  $3\sigma$  limiting values of  $\sin^2 \theta_{23}(\text{true})$ . A comparison of the broken lines with the corresponding continuous lines show the following feature. Matter effects tend to increase somewhat the sensitivity of ICAL to test the maximality of  $\sin^2 \theta_{23}$ .

We present in Table 4 the intervals of  $D(\text{true}) = 1/2 - \sin^2 \theta_{23}(\text{true})$  beyond which maximal mixing could be ruled out at the  $3\sigma$  level, with and without matter effects. The latter corresponds to a fictitious environment of pure vacuum and has been included to see the quantitative role of matter effects here. Specifically, for  $\Delta m_{31}^2(\text{true}) = 2.0 \times 10^{-3} \text{ eV}^2$  and  $\sin^2 \theta_{13}(\text{true}) = 0.04$  (0.00),  $\sin^2 \theta_{23}(\text{true})$  can be distinguished by ICAL from the maximal value of 0.5 at the  $3\sigma$  level within 17% (20%) from 1 MtonY of exposure and within 11% (14%) if the statistics was increased to 3.37 MtonY. The corresponding ranges of  $D(\text{true})$  are what Table 4 lists. This is comparable to the sensitivity of the combined data from the forthcoming accelerator-based long baseline experiments<sup>17</sup> to a deviation from maximality of  $\sin^2 \theta_{23}$ , which is [12]  $\sim 14\%$  at  $3\sigma$  (for  $\Delta m_{31}^2(\text{true}) = 2.5 \times 10^{-3} \text{ eV}^2$ )<sup>18</sup>. Our sensitivity to  $D$  is also comparable to that expected with atmospheric neutrinos in very large futuristic water Cerenkov detectors. For statistics that is 20 (50) times the current SK statistics, denoted as SK20 (SK50), a very large water Cerenkov atmospheric neutrino experiment is expected to test a deviation from a maximal  $\sin^2 \theta_{23}$  upto [9] 23% (19%) at  $3\sigma$ .

Let us make some observations here. While atmospheric neutrino data in a very large water Cerenkov detector could test [9] maximality in  $\sin^2 \theta_{23}$  almost independently of the values of  $\sin^2 \theta_{13}(\text{true})$  and  $\Delta m_{31}^2(\text{true})$ , the sensitivity at a detector like ICAL to  $D$  would depend on both these oscillation parameters. The dependence of the latter on  $\sin^2 \theta_{13}(\text{true})$  comes from the greater importance of matter effects here. The impact of  $\Delta m_{31}^2(\text{true})$  on the measurement  $D$  comes from the dependence of  $\sin^2 \theta_{23}$  sensitivity to the spectral shape of the data at ICAL, cf. §3. For a larger  $\Delta m_{31}^2(\text{true})$ , there is a larger averaging of the oscillation signal and the  $\sin^2 \theta_{23}$  sensitivity is reduced slightly. Such a fact is evident from Figs. 8 and 9 which display the muon ( $\mu^-$ ) zenith

<sup>15</sup>These are the bounds on the solar parameters expected from the future solar and long baseline reactor neutrino experiments. See for example [37] for a recent detailed discussion.

<sup>16</sup>3.37 MtonY would roughly be the statistics needed in ICAL to match the number of fully contained muon events in the experiment SK20 which is described later in this section.

<sup>17</sup>The authors of [12] use a combination of simulated data set from five years of running of MINOS, ICARUS, OPERA, T2K and NO $\nu$ A each, expected to come in the next ten years.

<sup>18</sup>This estimated uncertainty will be quite different if the true value of  $\Delta m_{31}^2$  deviates substantially from  $2.5 \times 10^{-3} \text{ eV}^2$ .

Range of $D$ (true) in units of $10^{-2}$						
	matter			vacuum		
$\sin^2 \theta_{13}$ (true)	0.00	0.02	0.04	0.00	0.02	0.04
1 MtonY	[9.8,-9.7]	[8.8,-10.3]	[8.4,-10.7]	[9.4,-9.4]	[9.2,-10.2]	[9.0,-11.1]
3.367 MtonY	[7.0,-7.0]	[5.9,-7.2]	[5.5,-7.2]	[6.6,-6.7]	[6.3,-7.3]	[6.0,-8.0]

Table 4: Simulated ranges of deviation  $D$  from maximal  $\sin^2 \theta_{23}$ , allowed at  $3\sigma$ , after two different exposure times at ICAL. Here  $\Delta m_{31}^2$ (true) has been taken to be  $2.0 \times 10^{-3}$ eV $^2$ .

angle spectrum for  $\Delta m_{31}^2 = 2.0 \times 10^{-3}$  eV $^2$  and  $4.0 \times 10^{-3}$  eV $^2$  respectively. The four panels in both figures show the zenith angle dependence of the muon events in four different energy bins which are labeled. While the solid black and the magenta dotted lines are for  $\sin^2 \theta_{23} = 0.5$  (maximal) and 0.4 respectively, the blue dot-dashed lines correspond to unoscillated neutrinos. A comparison between Figs. 8 and 9 reveals an interesting feature. The case with the higher value of  $\Delta m_{31}^2$  has a spectral distortion which is less than that with the lower value, especially when  $E$  is between 3 and 5 GeV and when  $E$  is between 5 and 7 GeV, which are statistically the most important energy bins. The reason is that the oscillations are faster for  $\Delta m_{31}^2 = 4.0 \times 10^{-3}$  eV $^2$ , leading to partial averaging and a smaller spectral distortion in the resultant signal. In fact, for the same reason, matter effects also are slightly more important for  $\Delta m_{31}^2 = 2.0 \times 10^{-3}$  eV $^2$ , as compared to the higher value quoted above. Such an increased averaging, especially in the statistically more relevant lower energy bins, results in a slight fall in the sensitivity of ICAL to the precision of the oscillation parameters. This happens since the use of spectral distortion is a crucial component of the latter in relation to oscillation parameters, including the deviation  $D$  from the maximality of  $\sin^2 \theta_{23}$ .

## 7 Sensitivity to the octant of $\theta_{23}$

We now come to the determination of the sign of  $D = 1/2 - \sin^2 \theta_{23}$  which decides whether  $\theta_{23} < \pi/4$  ( $D$  positive) or  $\theta_{23} > \pi/4$  ( $D$  negative), i.e. whether  $\theta_{23}$  lies in the first or second octant of the  $(0, 2\pi]$  range. In a two-generation picture, the dependence of the survival probability  $P_{\mu\mu}$  only on  $\sin^2 2\theta_{23}$  makes it impossible to fix the octant of  $\theta_{23}$ . Even in a three-generation framework, given that  $\theta_{13}$  and  $\alpha$  are small, the dominant part of  $P_{\mu\mu}$  in vacuum is still found to depend only on  $\sin^2 2\theta_{23}$ . Therefore, once again the fixation of the octant of  $\theta_{23}$  would be nearly impossible from a study of vacuum oscillations in surviving muon neutrinos. This degeneracy, however, is broken in matter owing to an additional strong  $\sin^4 \theta_{23}$  dependence in  $P_{\mu\mu}$ , as clear from the third term  $P_{\mu\mu}^3$  in Eq. (31). Since we have already demonstrated the significant potentiality of the ICAL-like detector in deciphering the effects of earth matter on its observed muon neutrino/antineutrino events, we expect such a detector to be sensitive to the octant of  $\theta_{23}$ . That is what we now numerically investigate.

The simulated event spectrum at this detector is first generated at some nonmaximal “true”

value of  $\theta_{23}$ . Then we try and see if the wrong octant of  $\theta_{23}$  can be ruled out at a good C.L. Here we use anticipated constraints on  $\sin^2 \theta_{13}$  from future reactor and long baseline experiments, but we have allowed all other parameters except  $\sin^2 \theta_{23}$  to vary freely in the fit. We consider three different cases of  $\sin^2 \theta_{23}(\text{true})$  values, namely 0.42, 0.46 and 0.54. The “true” values of the other oscillation parameters are as listed in Table 2 with an assumed normal mass ordering. Fig. 10 shows the results of our statistical analysis based on simulated data from 1 MtonY of ICAL exposure with the left, middle and right panels corresponding to the values 0.42, 0.46 and 0.54 respectively of  $\sin^2 \theta_{23}(\text{true})$ . In each panel the long dashed magenta, short dashed blue, dot-dashed green, dotted red and solid black lines show the  $\chi^2$  for  $\sin^2 \theta_{13}(\text{true}) = 0.00, 0.01, 0.02, 0.03$  and 0.04 respectively. For every nonmaximal  $\sin^2 \theta_{23}(\text{true})$ , there exists a  $\sin^2 \theta_{23}(\text{false})$  which is given by

$$\sin^2 \theta_{23}(\text{false}) = 1 - \sin^2 \theta_{23}(\text{true}) \quad (42)$$

on the other side of  $\pi/4$ . For a vanishing  $\sin^2 \theta_{13}(\text{true})$  there are no matter effects and the  $\chi^2$  corresponding to both the true and false values of  $\sin^2 \theta_{23}$  are the same. Hence they are allowed at the same C.L. and one fails to fix the octant of  $\theta_{23}$  in this case. However, for  $\sin^2 \theta_{13}(\text{true}) \neq 0$ , matter effects bring in an octant sensitivity and a false  $\sin^2 \theta_{23}$  solution can be ruled out, provided  $D(\text{true})$  is not too close to zero. For a given  $\sin^2 \theta_{13}(\text{true})$ , the C.L. at which this can be done for our illustrative cases of  $\sin^2 \theta_{23}(\text{true})$  can be read out using Fig. 10, from the difference in the  $\chi^2$  between the true and false solutions.

In order to obtain the limiting value of  $\sin^2 \theta_{23}(\text{true})$  which could still allow for the determination of  $\text{sgn}(D)$  we define

$$\begin{aligned} \Delta\chi^2 \equiv & \chi^2(\sin^2 \theta_{23}(\text{true}), \sin^2 \theta_{13}(\text{true}), \text{others}(\text{true})) \\ & - \chi^2(\sin^2 \theta_{23}(\text{false}), \sin^2 \theta_{13}, \text{others}), \end{aligned} \quad (43)$$

with ‘others’ comprising  $\Delta m_{31}^2$ ,  $\Delta m_{21}^2$ ,  $\sin^2 \theta_{12}$  and  $\delta$ . These, along with  $\sin^2 \theta_{13}$ , are allowed to vary freely in the fit. Eq. (43) gives us a measure of the C.L. at which  $\sin^2 \theta_{23}(\text{false})$  is disfavored for a given  $\sin^2 \theta_{23}(\text{true})$ . Fig. 11 shows  $\Delta\chi^2$  as a function of  $\sin^2 \theta_{23}(\text{true})$  for four values 0.01, 0.02, 0.03 and 0.04 of  $\sin^2 \theta_{13}(\text{true})$ , corresponding respectively to the blue dashed, and green dot-dashed, the red dotted and the black solid lines. The left hand panel shows the results for a normal mass ordering of neutrinos while the right hand panel corresponds to the situation if the mass ordering for the neutrinos were inverted. The range of  $\sin^2 \theta_{23}(\text{true})$ , for which  $\sin^2 \theta_{23}(\text{false})$  can be ruled out at the  $3\sigma$  level, is visible from the figure. In particular, for a normal neutrino mass ordering,  $\sin^2 \theta_{23}(\text{false})$  should be excludable at the  $3\sigma$  level from 1 MtonY of ICAL exposure for the following cases:

$$\sin^2 \theta_{23}(\text{true}) < 0.361 \text{ or } > 0.633 \text{ for } \sin^2 \theta_{13}(\text{true}) = 0.01, \quad (44)$$

$$\sin^2 \theta_{23}(\text{true}) < 0.402 \text{ or } > 0.592 \text{ for } \sin^2 \theta_{13}(\text{true}) = 0.02, \quad (45)$$

$$\sin^2 \theta_{23}(\text{true}) < 0.415 \text{ or } > 0.580 \text{ for } \sin^2 \theta_{13}(\text{true}) = 0.03, \quad (46)$$

$$\sin^2 \theta_{23}(\text{true}) < 0.421 \text{ or } > 0.573 \text{ for } \sin^2 \theta_{13}(\text{true}) = 0.04. \quad (47)$$

For an inverted mass ordering, the sensitivity of ICAL to  $sgn(D)$  is seen to be slightly less from Fig. 11. This is the result of the following fact. When the mass ordering is inverted, larger matter effects appear for  $\bar{\nu}_\mu$ 's instead of  $\nu_\mu$ 's at baseline lengths  $L > 1000$  km. Owing to smaller interaction cross-sections for the antineutrinos, we roughly expect only half as many  $\bar{\nu}_\mu$ -induced antimuon events in the detector as compared with  $\nu_\mu$ -induced muon events. Therefore, the statistical power of the experiment for deciphering  $sgn(D)$  goes down by roughly a factor of half in this case.

In order to quantify the importance of distinguishing the  $\nu_\mu$ -induced muon events from the  $\bar{\nu}_\mu$ -induced antimuon events by means of the magnetic field in the detector, we have repeated our  $\chi^2$  analysis by “switching off” the magnetic field – or in other words by taking the sum of the muon and antimuon events in each bin. Therefore, in this case we have just a 60 bin data. Such a non-magnetized iron detector could then rule out the fake octant solution at  $3\sigma$  level for the normal mass ordering if  $\sin^2 \theta_{23}(\text{true}) < 0.372 (> 0.625)$  for  $\sin^2 \theta_{13}(\text{true}) = 0.04$  or  $\sin^2 \theta_{23}(\text{true}) < 0.398 (> 0.600)$  for  $\sin^2 \theta_{13}(\text{true}) = 0.04$ . It is not surprising that the potential to rule out the fake octant deteriorates significantly in this case, since the matter effects crucial for the octant sensitivity get diluted if neutrino and antineutrino events were added together. Distinguishing the neutrinos from the antineutrinos is therefore extremely important for the physics potential of experiments sensitive to large matter effects.

## 8 Discussions and conclusions

The measurement of both the magnitude and sign of the deviation  $D$  of  $\sin^2 \theta_{23}$  from its maximal value 0.5 is of utmost theoretical importance. The best current limit on this parameter  $D$  comes from the SK atmospheric neutrino experiment giving  $|D| \leq 0.16$  at the  $3\sigma$  level [5]. More precise measurements of  $\theta_{23}$  and hence of  $D$  are expected from future atmospheric neutrino data both from the currently running SK experiment and from the planned Megaton water Cerenkov detectors. Significantly better constraints are expected from data that will emerge from forthcoming long baseline experiments, owing to their larger statistics and lower systematic errors. However, in both these classes of experiments,  $\theta_{23}$  will be mainly determined by the  $\nu_\mu$  (and/or  $\bar{\nu}_\mu$ ) disappearance channel in vacuum, which predominantly depends on  $\sin^2 2\theta_{23}$ . This leads to two very important consequences. The first one relates to the fact that the mixing angle  $\theta_{23}$  is very close to being maximal. The fact that  $\delta(\sin^2 \theta_{23})$  equals  $\delta(\sin^2 2\theta_{23})/(4 \cos 2\theta_{23})$  has the following implication. Even though one could determine the value of  $\sin^2 2\theta_{23}$  at the percentage level from the next generation long baseline experiments, the uncertainty in  $\sin^2 \theta_{23}$  would still remain in the region of 10-20%, depending on  $\sin^2 \theta_{23}(\text{true})$ . The second consequence of the predominant  $\sin^2 2\theta_{23}$  dependence of the disappearance probability in long baseline experiments means that they are almost insensitive to the octant of  $\theta_{23}$  and hence to the sign of  $D$ .

In this paper we have argued in a quantitative way that the presence of matter effects in the neutrino survival probability enhances its sensitivity to  $\theta_{23}$ . In particular, we have shown that the strong  $\sin^2 \theta_{23}$  dependence of the matter effects in  $P_{\mu\mu}$  can be used to increase the sensitivity of  $\nu_\mu$ 's and  $\bar{\nu}_\mu$ 's disappearance experiments to  $D$ . Using the signal for atmospheric  $\nu_\mu$  and  $\bar{\nu}_\mu$  in a large magnetized iron calorimetric detector like the planned ICAL at INO in India, we have

demonstrated the following fact: for large enough values of  $\sin^2 \theta_{13}(\text{true})$ , the detection of matter effects in the data would be feasible and would lead to better constraints on  $|D|$ . Appropriate binning of the data in both energy and zenith angle holds the key to the observation of matter effects in the resultant signal. We have distributed our simulated events into twelve zenith angle bins covering both up and down going neutrinos – each of which was then further divided into five energy bins, giving us sixty bins of data. The charge discrimination capability of a magnetized detector like ICAL will allow the separation between  $\nu_\mu$ - and  $\bar{\nu}_\mu$ -induced events. Hence we have simulated separate data sets for  $\nu_\mu$ 's and  $\bar{\nu}_\mu$ 's. Since for a given neutrino mass ordering, substantial matter effects appear in only either the neutrino or the antineutrino channel, the effective use of separate data sets for  $\nu_\mu$  and  $\bar{\nu}_\mu$  will enable the extraction of matter effects in the survival probability through a statistical analysis. We have defined a  $\chi^2$  function to analyze the data set expected from atmospheric neutrino events collected in an ICAL-like detector and presented the C.L. limits on  $|D|$ . We have noted that the presence of matter effects increase the sensitivity of ICAL to  $|D|$  somewhat. For  $\sin^2 \theta_{13}(\text{true}) = 0.04$ , matter effects are seen to improve the  $3\sigma$  limit on  $|D|$  from 0.090 to 0.084. We expect to measure  $|D|$  within 18% (17%) at  $3\sigma$  with 1 MtonY data when  $\sin^2 \theta_{13}(\text{true}) = 0.02$  (0.04). This is comparable to the limit on  $|D|$  expected from the forthcoming long baseline experiments and slightly better than what is expected from atmospheric neutrino experiments with Megaton water Cerenkov detectors.

Matter effects in  $P_{\mu\mu}$  open up a new utility for an ICAL-like detector – sensitivity to the octant of  $\theta_{23}$ . As is well known, the atmospheric neutrino data set collected so far by the SK experiment constrains the atmospheric neutrino mixing angle in the form  $\sin^2 2\theta_{23}$  and is hence insensitive to the octant of  $\theta_{23}$  if its true value were non-maximal. This ambiguity in whether  $\theta_{23}$  is smaller or greater than  $\pi/4$  leads to an additional two-fold degeneracy [38] in the measurement of the mixing angle  $\theta_{13}$  and the CP phase  $\delta$  in long baseline experiments, looking for electron neutrino appearance in an original muon neutrino beam through the  $P_{\mu e}$  channel which depends on  $\sin^2 \theta_{23}$  and hence to the octant of  $\theta_{23}$ . The  $P_{\mu\mu}$  channel in the long baseline experiments, which is expected to give the best limits on  $\theta_{23}$ , is almost insensitive to its octant [15]. The proposed ways to tackle the  $\theta_{23}$  octant ambiguity in the determination of  $\theta_{13}$  and  $\delta$  in long baseline experiments include (1) combining the data from the  $P_{\mu e}$  (or  $P_{e\mu}$ ) channel of the long baseline experiment with data from the next generation reactor experiments [34], (2) combining the data from the  $P_{\mu e}$  (or  $P_{e\mu}$ ) channel of the long baseline experiments with different energies and baseline lengths and (3) combined studies of the  $P_{\mu e}$  or  $P_{e\mu}$  (golden) and the  $P_{e\tau}$  (silver) channels [39].

The octant ambiguity can be resolved from a direct measurement of the sign of  $D$  utilizing atmospheric neutrino data. It was shown in [9] that the atmospheric neutrino data in SK like experiments could be sensitive to the octant of  $\theta_{23}$  through the  $\Delta m_{21}^2$  driven sub-dominant oscillations. The latter are sizable for very small values of the neutrino energies and result in an excess in the sub-GeV electron sample in Megaton water Cerenkov detectors. They conclude that, with a statistics fifty times the current SK statistics, this effect can be used to determine the correct octant of  $\theta_{23}$  at the  $3\sigma$  level if the true value  $\sin^2 \theta_{23}(\text{true}) < 0.36$  or  $> 0.62$ . We have shown in this paper that for large enough  $\sin^2 \theta_{13}(\text{true})$ , the observation of matter effects in atmospheric neutrinos in an ICAL like detector could be used very efficiently to determine the octant of  $\theta_{23}$ . The observation of significant matter effects in  $P_{\mu\mu}$  allows the rejection of the false octant solution of  $\theta_{23}$  at the  $3\sigma$  level for  $\sin^2 \theta_{23}(\text{true}) < 0.40$  ( $< 0.42$ ) or  $\sin^2 \theta_{23}(\text{true}) > 0.59$

( $> 0.57$ ) for  $\sin^2 \theta_{13}(\text{true}) = 0.02$  ( $0.04$ ) with 1 MtonY statistics in ICAL, given a normal neutrino mass ordering. For an inverted mass ordering, the false  $\theta_{23}$  can be rejected at the  $3\sigma$  level for  $\sin^2 \theta_{23}(\text{true}) < 0.37$  ( $< 0.40$ ) or  $\sin^2 \theta_{23}(\text{true}) > 0.62$  ( $> 0.60$ ) for  $\sin^2 \theta_{13}(\text{true}) = 0.02$  ( $0.04$ ). The sensitivity to  $\text{sgn}(D)$  in ICAL is therefore slightly less for an inverted mass ordering than for a normal one. But it is still better than what is expected from other experiments. Hence, using matter effects to pick the right octant in an INO-like experiment seems to be the most promising way of resolving the  $\theta_{23}$  octant ambiguity by determining the sign of  $D$ .

We thank S. R. Dugad, S. Goswami, M. V. N. Murthy, D. P. Roy and A. Raychaudhuri for their helpful comments.

## References

- [1] Y. Ashie *et al.* [Super-Kamiokande Collaboration], Phys. Rev. Lett. **93**, 101801 (2004).
- [2] E. Aliu *et al.* [K2K Collaboration], Phys. Rev. Lett. **94**, 081802 (2005).
- [3] B. Aharmim *et al.* [SNO Collaboration], Phys. Rev. C **72**, 055502 (2005).
- [4] T. Araki *et al.* [KamLAND Collaboration], Phys. Rev. Lett. **94**, 081801 (2005).
- [5] Y. Ashie *et al.* [Super-Kamiokande Collaboration], Phys. Rev. D **71**, 112005 (2005).
- [6] S. Fukuda *et al.* [Super-Kamiokande Collaboration], Phys. Lett. B **539**, 179 (2002); Q. R. Ahmad *et al.* [SNO Collaboration], Phys. Rev. Lett. **89**, 011301 (2002); Q. R. Ahmad *et al.* [SNO Collaboration], Phys. Rev. Lett. **89**, 011302 (2002); B. T. Cleveland *et al.*, Astrophys. J. **496**, 505 (1998); J. N. Abdurashitov *et al.* [SAGE Collaboration], J. Exp. Theor. Phys. **95**, 181 (2002) [Zh. Eksp. Teor. Fiz. **122**, 211 (2002)]; W. Hampel *et al.* [GALLEX Collaboration], Phys. Lett. B **447**, 127 (1999); C. Cattadori, Talk at Neutrino 2004, Paris, France, June 14-19, 2004.
- [7] S. Goswami, A. Bandyopadhyay and S. Choubey, Nucl. Phys. Proc. Suppl. **143**, 121 (2005); A. Bandyopadhyay *et al.*, Phys. Lett. B **608**, 115 (2005); A. Strumia and F. Vissani, arXiv:hep-ph/0503246. G. L. Fogli *et al.*, arXiv:hep-ph/0506083; M. Maltoni *et al.*, New J. Phys. **6**, 122 (2004).
- [8] M. Apollonio *et al.*, Eur. Phys. J. C **27**, 331 (2003).
- [9] M. C. Gonzalez-Garcia, M. Maltoni and A. Y. Smirnov, Phys. Rev. D **70**, 093005 (2004).
- [10] R. N. Mohapatra and W. Rodejohann, arXiv:hep-ph/0507312 and references therein.
- [11] M. Raidal, Phys. Rev. Lett. **93**, 161801 (2004); H. Minakata and A. Y. Smirnov, Phys. Rev. D **70**, 073009 (2004); J. Ferrandis and S. Pakvasa, Phys. Rev. D **71**, 033004 (2005); S. Antusch, S. F. King and R. N. Mohapatra, Phys. Lett. B **618**, 150 (2005).

- [12] S. Antusch *et al.*, Phys. Rev. D **70**, 097302 (2004) and references therein.
- [13] H. Minakata, M. Sonoyama and H. Sugiyama, Phys. Rev. D **70**, 113012 (2004).
- [14] T. Kajita, talk at the *5th workshop on neutrino oscillations and their origin*, <http://www-sk.icrr.u-tokyo.ac.jp/noon2004/>; C.K. Jung, hep-ex/0005046, L. Mosca, talk at the *Villars CERN/SPSC meeting*, <http://nuspp.in2p3.fr/Frejus>.
- [15] P. Huber, M. Maltoni and T. Schwetz, Phys. Rev. D **71**, 053006 (2005).
- [16] J. Bernabeu, S. Palomares Ruiz and S. T. Petcov, Nucl. Phys. B **669**, 255 (2003) and references therein.
- [17] R. Gandhi *et al.* arXiv:hep-ph/0506145.
- [18] <http://www.imsc.res.in/~ino/>
- [19] S. Palomares-Ruiz and S. T. Petcov, Nucl. Phys. B **712**, 392 (2005).
- [20] D. Indumathi and M. V. N. Murthy, Phys. Rev. D **71**, 013001 (2005).
- [21] R. Gandhi *et al.*, Phys. Rev. Lett. **94**, 051801 (2005); R. Gandhi *et al.*, arXiv:hep-ph/0411252.
- [22] A.M. Dziewonski and D.L. Anderson, Phys. Earth Planet Inter. **25** 297 (1981); S.V. Panasyuk, Reference Earth Model (REM) webpage, <http://cfaunes5.harvard.edu/lana/rem/index.html>.
- [23] B. Pontecorvo, Sov. Phys. JETP **6**, 429 (1957) [Zh. Eksp. Teor. Fiz. **33**, 549 (1957)]; B. Pontecorvo, Sov. Phys. JETP **7**, 172 (1958) [Zh. Eksp. Teor. Fiz. **34**, 247 (1957)]; Z. Maki, M. Nakagawa and S. Sakata, Prog. Theor. Phys. **28**, 870 (1962).
- [24] E. K. Akhmedov *et al.*, JHEP **0404**, 078 (2004).
- [25] S. Choubey and P. Roy, Phys. Rev. Lett. **93**, 021803 (2004). B. Brahmachari, S. Choubey and P. Roy, Nucl. Phys. **B671**, 483 (2003).
- [26] T. Kajita, New J. Phys. **6**, 194 (2004); O. L. G. Peres and A. Y. Smirnov, Phys. Lett. B **456**, 204 (1999); O. L. G. Peres and A. Y. Smirnov, Nucl. Phys. B **680**, 479 (2004).
- [27] G. L. Fogli *et al.*, Phys. Rev. D **55**, 4385 (1997); C. Giunti, C. W. Kim and M. Monteno, Nucl. Phys. B **521**, 3 (1998).
- [28] M. Honda *et al.*, Phys. Rev. D **70**, 043008 (2004).
- [29] Y. Fukuda *et al.* [Super-Kamiokande Collaboration], Phys. Rev. Lett. **81**, 1562 (1998).
- [30] <http://user.pa.msu.edu/wkt/cteq/cteq6/cteq6pdf.html>
- [31] M. C. Gonzalez-Garcia and M. Maltoni, Phys. Rev. D **70**, 033010 (2004).

- [32] G. L. Fogli *et al.*, Phys. Rev. D **67**, 093006 (2003).
- [33] Masaki Ishitsuka, PhD Thesis, University of Tokyo, Feb., 2004, <http://www-sk.icrr.u-tokyo.ac.jp/doc/sk/pub/>; Jun Kameda, PhD Thesis, University of Tokyo, Sep. 2002, <http://www-sk.icrr.u-tokyo.ac.jp/doc/sk/pub/>.
- [34] K. Anderson *et al.*, arXiv:hep-ex/0402041.
- [35] E. Ables *et al.* [MINOS Collaboration], FERMILAB-PROPOSAL-0875 (1995); P. Aprili *et al.* [ICARUS Collaboration], CERN-SPSC-2002-027 (2002); M. Guler *et al.* [OPERA Collaboration], CERN-SPSC-2000-028 (2000); Y. Itow *et al.*, arXiv:hep-ex/0106019. D. S. Ayres *et al.* [NOvA Collaboration], arXiv:hep-ex/0503053.
- [36] P. Huber *et al.*, Phys. Rev. D **70**, 073014 (2004).
- [37] A. Bandyopadhyay *et al.*, Phys. Rev. D **72**, 033013 (2005); A. Bandyopadhyay, S. Choubey and S. Goswami, Phys. Rev. D **67**, 113011 (2003).
- [38] G. L. Fogli and E. Lisi, Phys. Rev. D **54**, 3667 (1996).
- [39] O. Yasuda, Nucl. Phys. Proc. Suppl. **149**, 170 (2005).

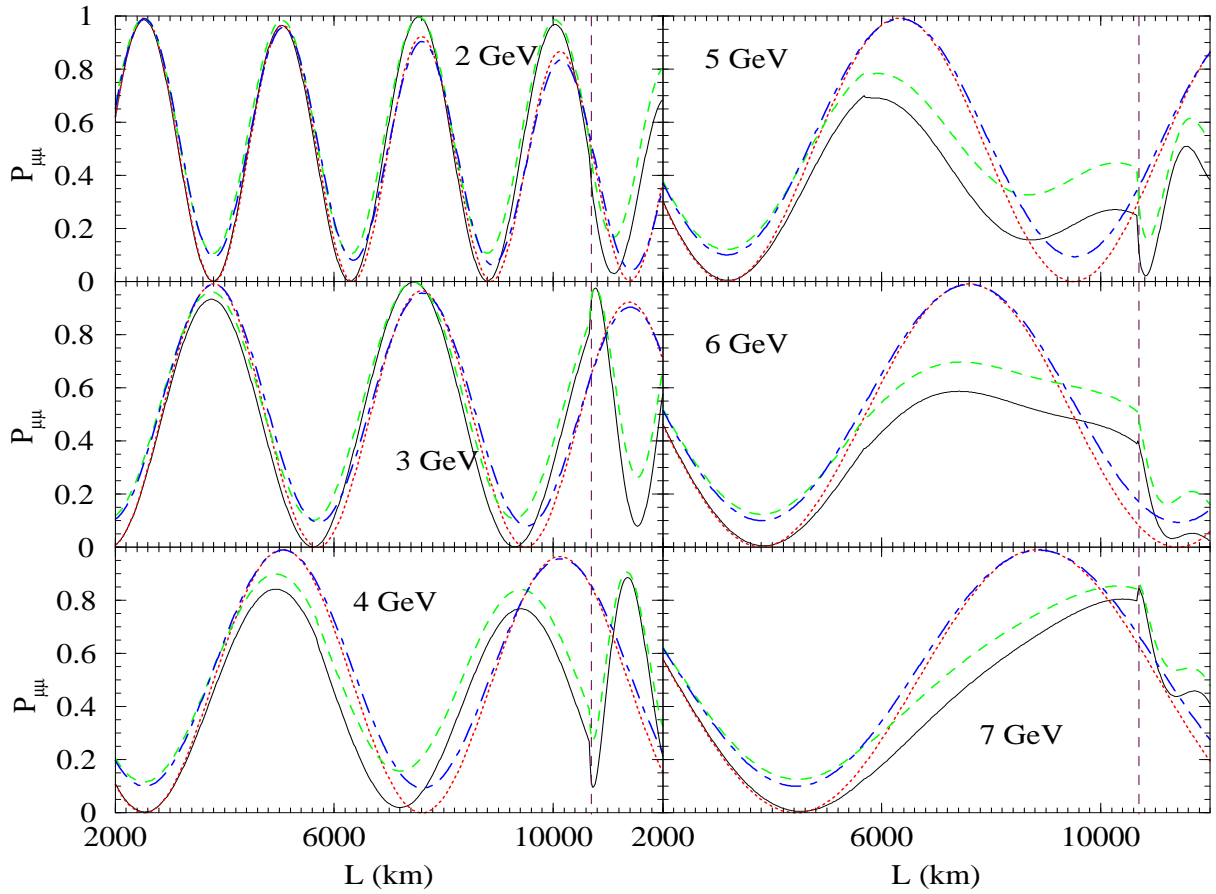


Figure 1:  $P_{\mu\mu}$  as a function of  $L$  with fixed  $E$  (and at various values of  $E$ ) for neutrinos travelling in vacuum and matter. The black solid lines and the dashed green lines are for propagation in matter with  $\sin^2 \theta_{23} = 0.5$  and  $0.36$  respectively. The red dotted lines and the blue dot-dashed lines are for that in vacuum for the same respective values of  $\sin^2 \theta_{23}$ . The vertical dashed lines represent the mantle-core boundary inside the earth.

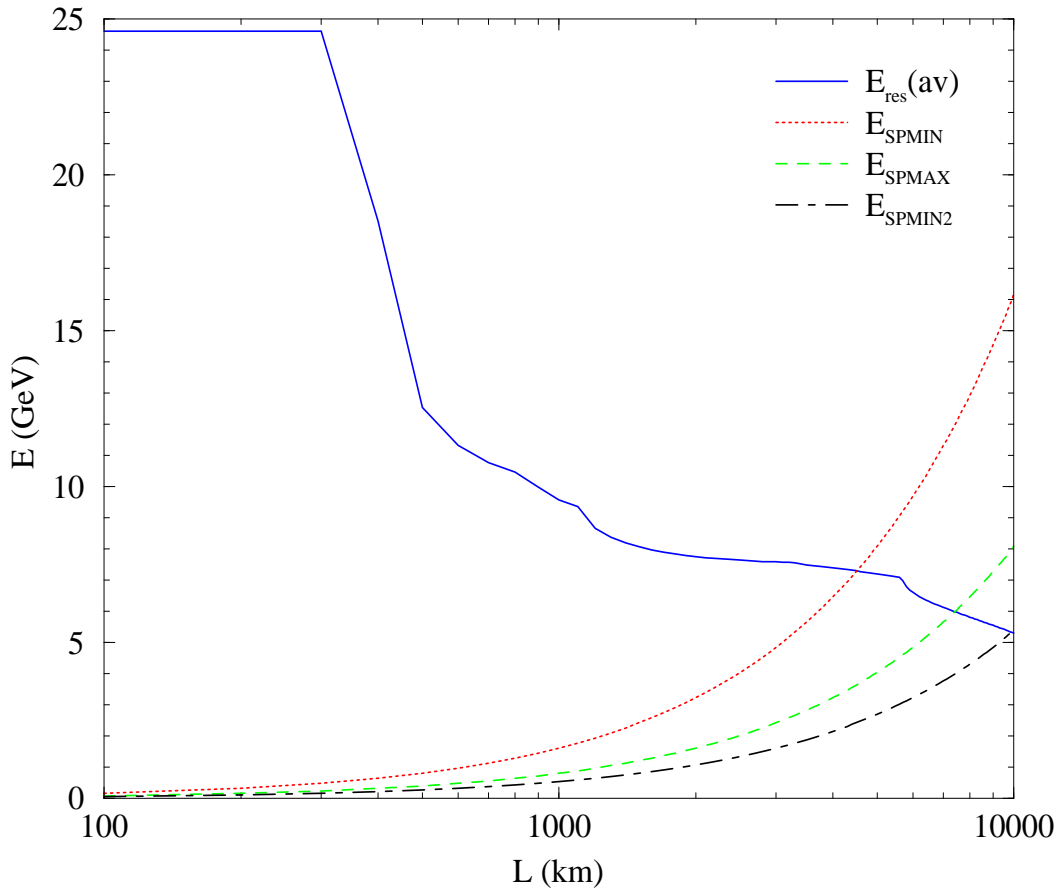


Figure 2: The average  $E_{res}$  (blue solid line) as a function of the baseline length in earth. Also shown are  $E_{SPMIN}$  (red dotted line),  $E_{SPMAX}$  (green dashed line) and  $E_{SPMIN2}$  (black dot-dashed line) in vacuum. They curve owing to the logarithmic scale of the horizontal axis.

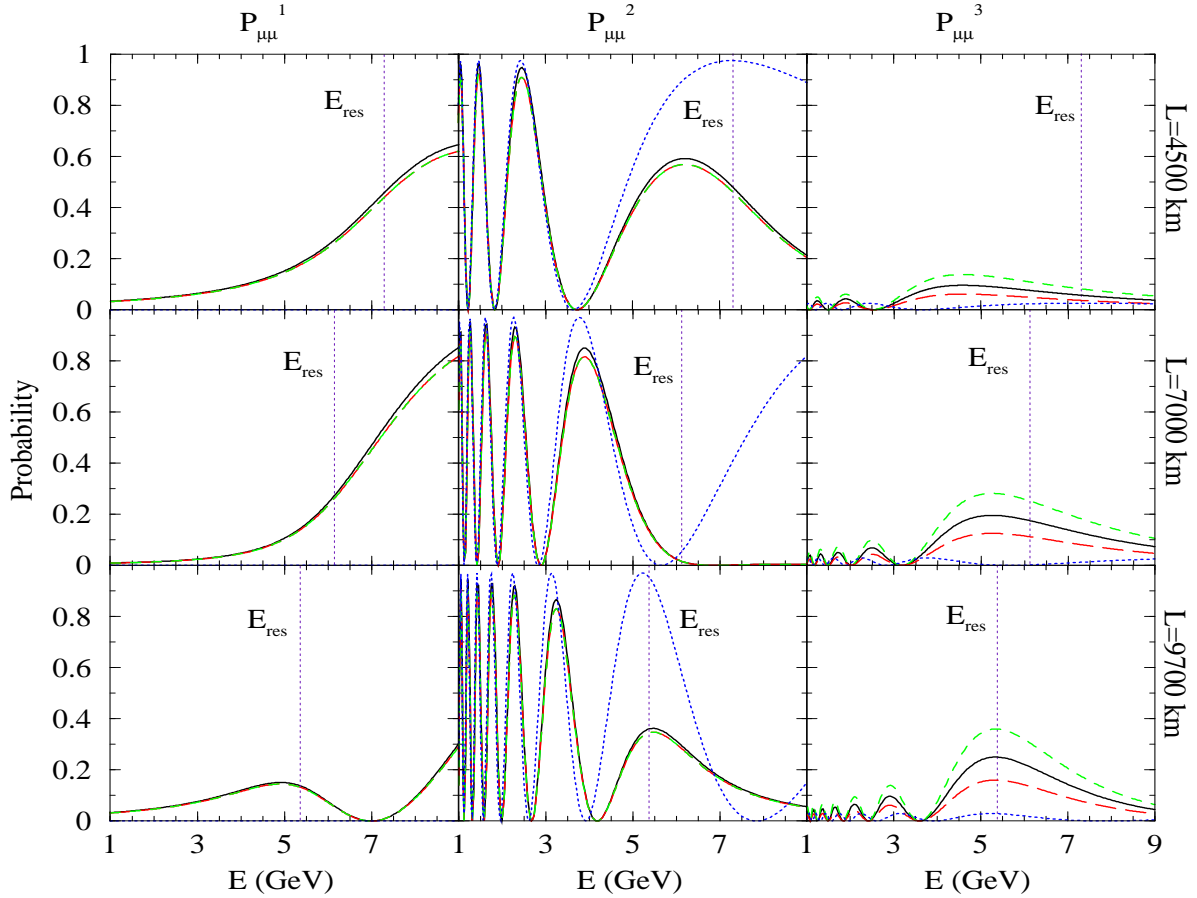


Figure 3: Plots of  $P_{\mu\mu}^{1,2,3}$ , the notional quantities of Eq. (27) defined in the limit  $\alpha \rightarrow 0$ , as functions of the neutrino energy  $E$  with a fixed baseline length  $L$  for different  $L$ -values as shown. The black solid lines, red long-dashed lines and green dashed lines correspond to  $\nu_\mu$ 's travelling in matter with  $\sin^2 \theta_{23} = 0.5, 0.4$  and  $0.6$  respectively and the blue dotted lines to the same in vacuum with  $\sin^2 \theta_{23} = 0.5$ .

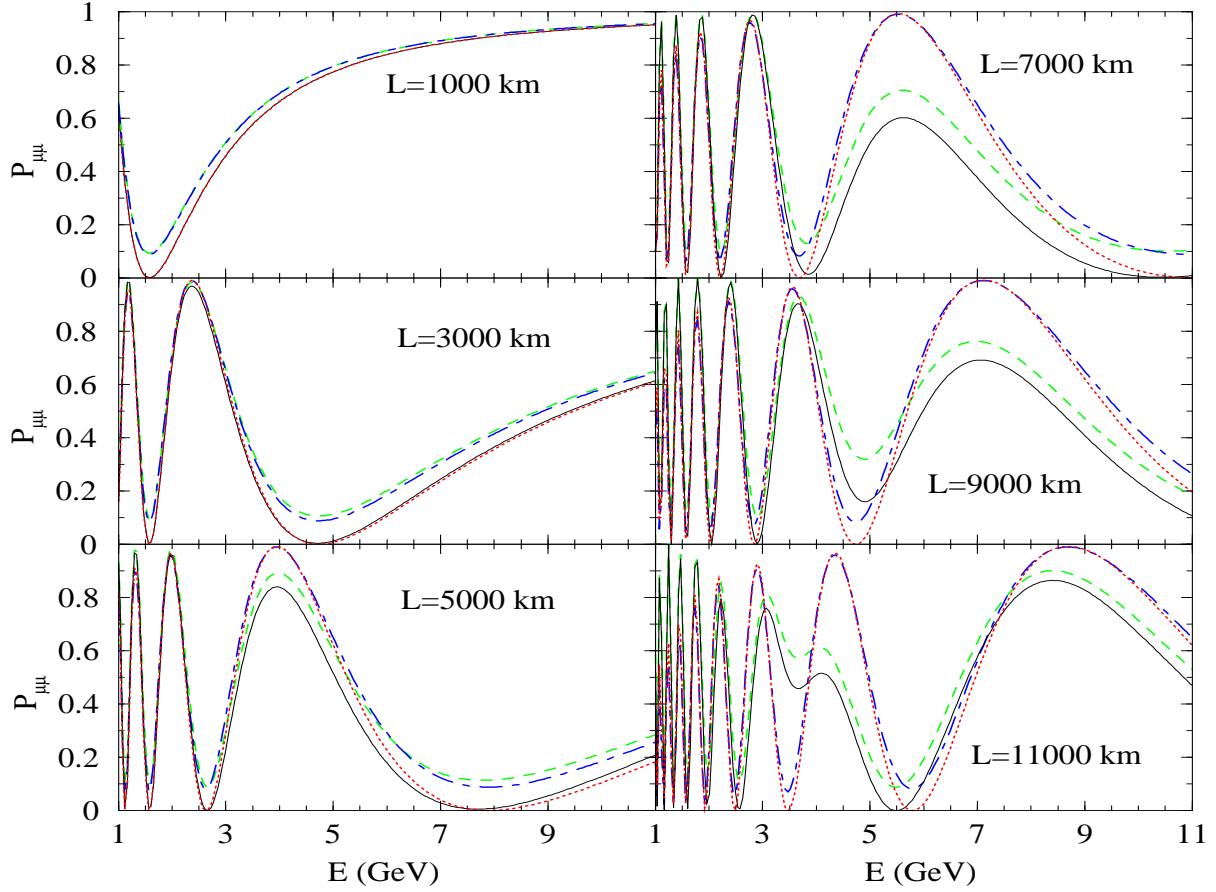


Figure 4:  $P_{\mu\mu}$  as a function of  $E$  for fixed values of  $L$ . The black solid and the dashed green lines are for neutrinos travelling in matter with  $\sin^2 \theta_{23} = 0.5$  and  $\sin^2 \theta_{23} = 0.36$  respectively. The red dotted and the blue dot-dashed lines show the corresponding respective cases in vacuum.

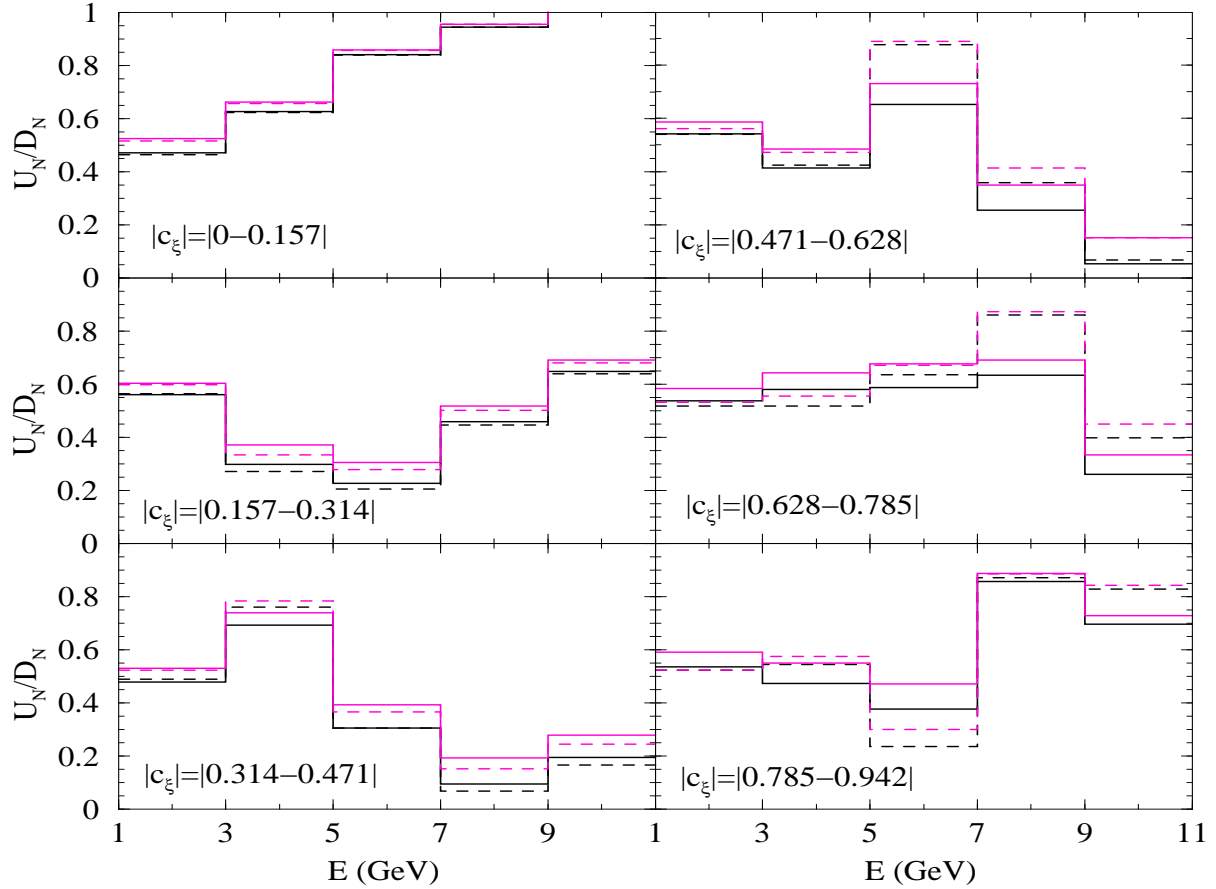


Figure 5: The up-down asymmetry expected for muon neutrinos in energy bins of width 2 GeV. The six panels show the data for six different zenith angle (or  $L$ ) bins corresponding to upward neutrinos travelling between  $L_m = 0 - 2000$  km,  $L_m = 2000 - 4000$  km,  $L_m = 4000 - 6000$  km,  $L_m = 6000 - 8000$  km,  $L_m = 8000 - 10000$  km and  $L_m = 10000 - 12000$  km respectively inside the earth, cf. Table 3. The solid black lines and the solid magenta lines are for neutrinos travelling in matter with  $\sin^2 \theta_{23} = 0.5$  and 0.36 respectively. The dashed black lines and the dashed magenta lines are for neutrinos travelling in vacuum with  $\sin^2 \theta_{23} = 0.5$  and 0.36 respectively. For all cases we have taken  $\Delta m_{31}^2 = 2 \times 10^{-3}$  eV $^2$  and the benchmark values of Table 2 for the other parameters.

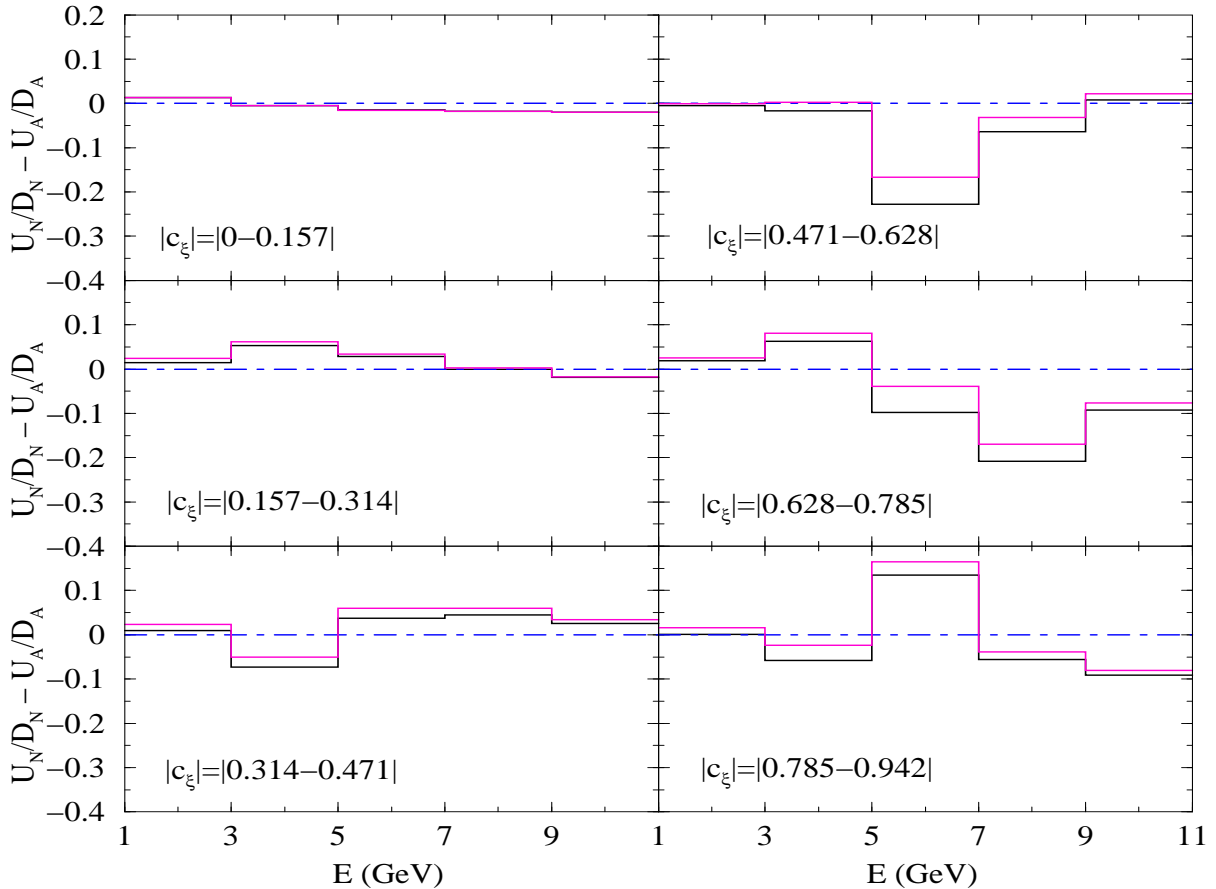


Figure 6: The difference between the up-down ratio for the neutrinos ( $U_N/D_N$ ) and antineutrinos ( $U_A/D_A$ ) shown for the various energy and zenith angle bins. The solid black lines are for neutrinos/antineutrinos travelling in matter with  $\sin^2 \theta_{23} = 0.5$ , while the solid magenta lines are neutrinos/antineutrinos travelling in matter with  $\sin^2 \theta_{23} = 0.36$ . The dot-dashed blue line shows  $U_N/D_N - U_A/D_A = 0$  for reference. The other oscillation parameters are chosen as in Fig. 5.

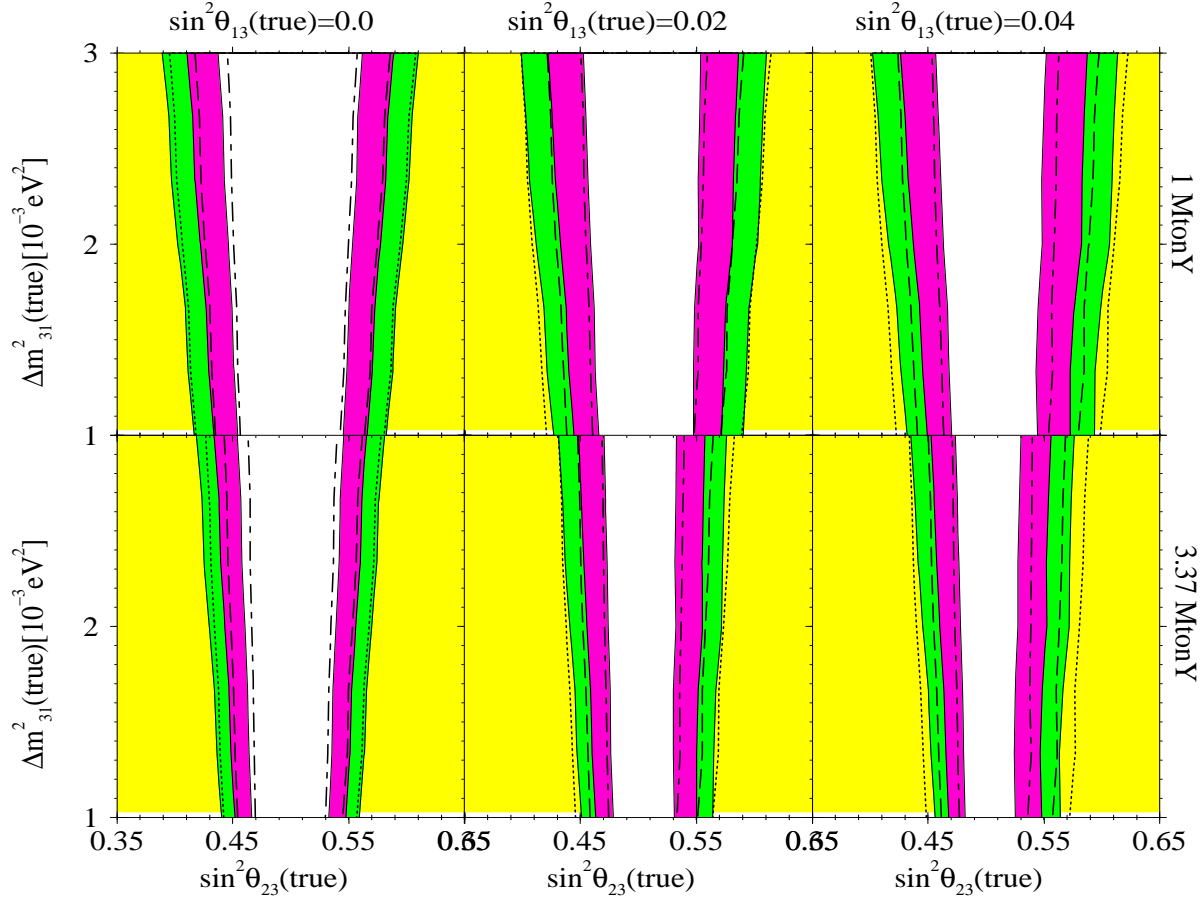


Figure 7: The regions of  $\Delta m_{31}^2(\text{true})$  and  $\sin^2 \theta_{23}(\text{true})$  where maximal  $\theta_{23}$  mixing can be rejected by using 1 MtonY (upper panels) and 3.37 MtonY (lower panels) atmospheric neutrino data in ICAL at  $1\sigma$  (white band),  $2\sigma$  (blue band) and  $3\sigma$  (green band). The hollow dark lines show the corresponding bands for neutrinos travelling in pure vacuum. Benchmark parametric values of Table 2 have been assumed.

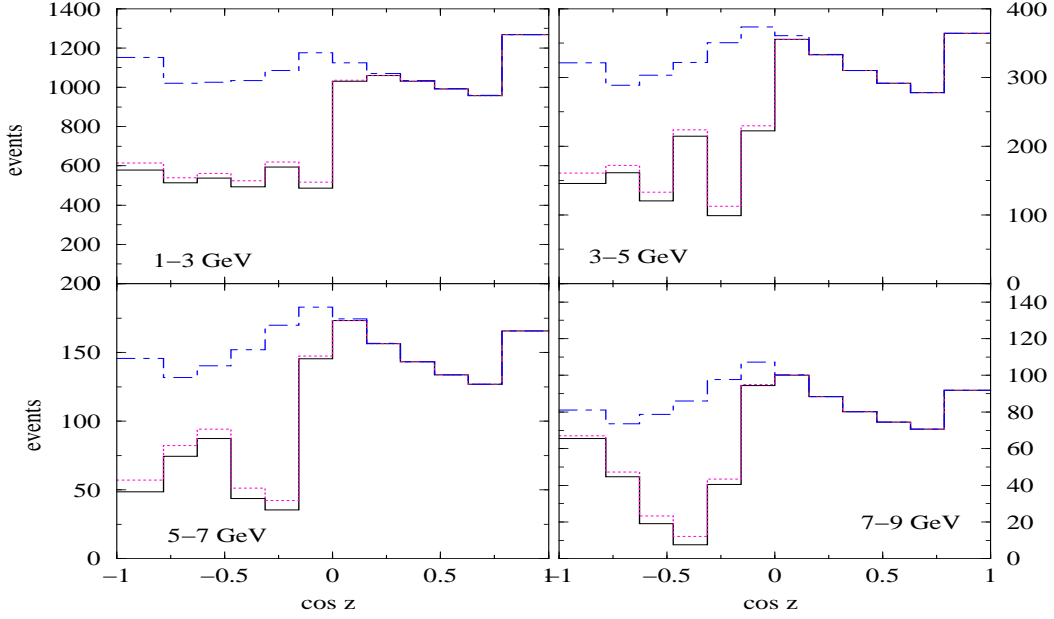


Figure 8: The zenith angle distribution of muon events for four energy bins shown in the four panels and for  $\Delta m_{31}^2 = 2 \times 10^{-3} \text{ eV}^2$ . The black solid lines show the events for maximal  $\sin^2 \theta_{23}$ , the dotted magenta lines show the events for  $\sin^2 \theta_{23} = 0.4$  and the blue dot-dashed lines show the events for the unoscillated flux.

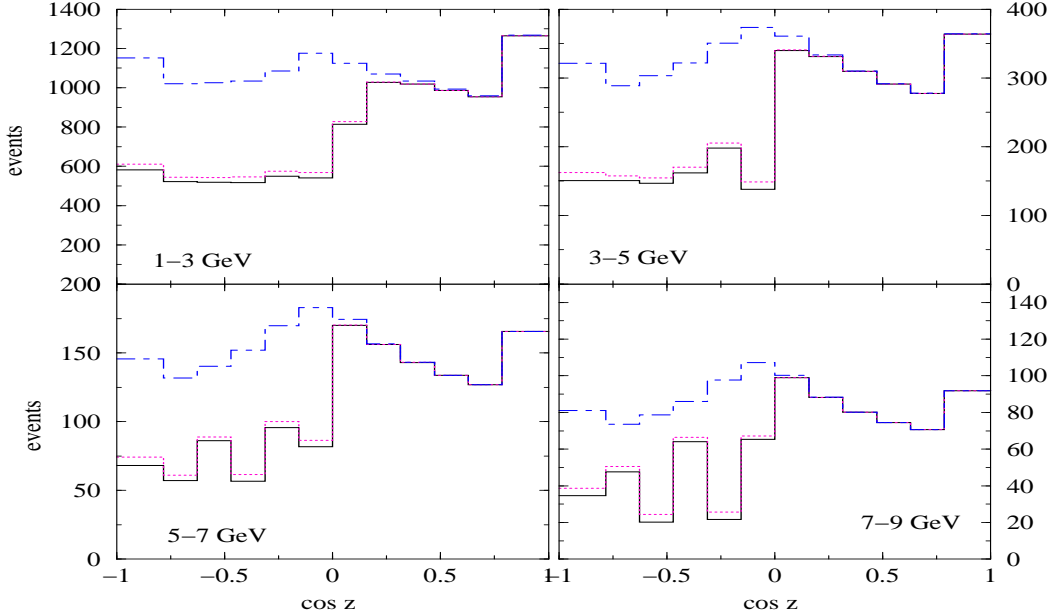


Figure 9: Same as Fig. 8, but for  $\Delta m_{31}^2 = 4 \times 10^{-3} \text{ eV}^2$ .

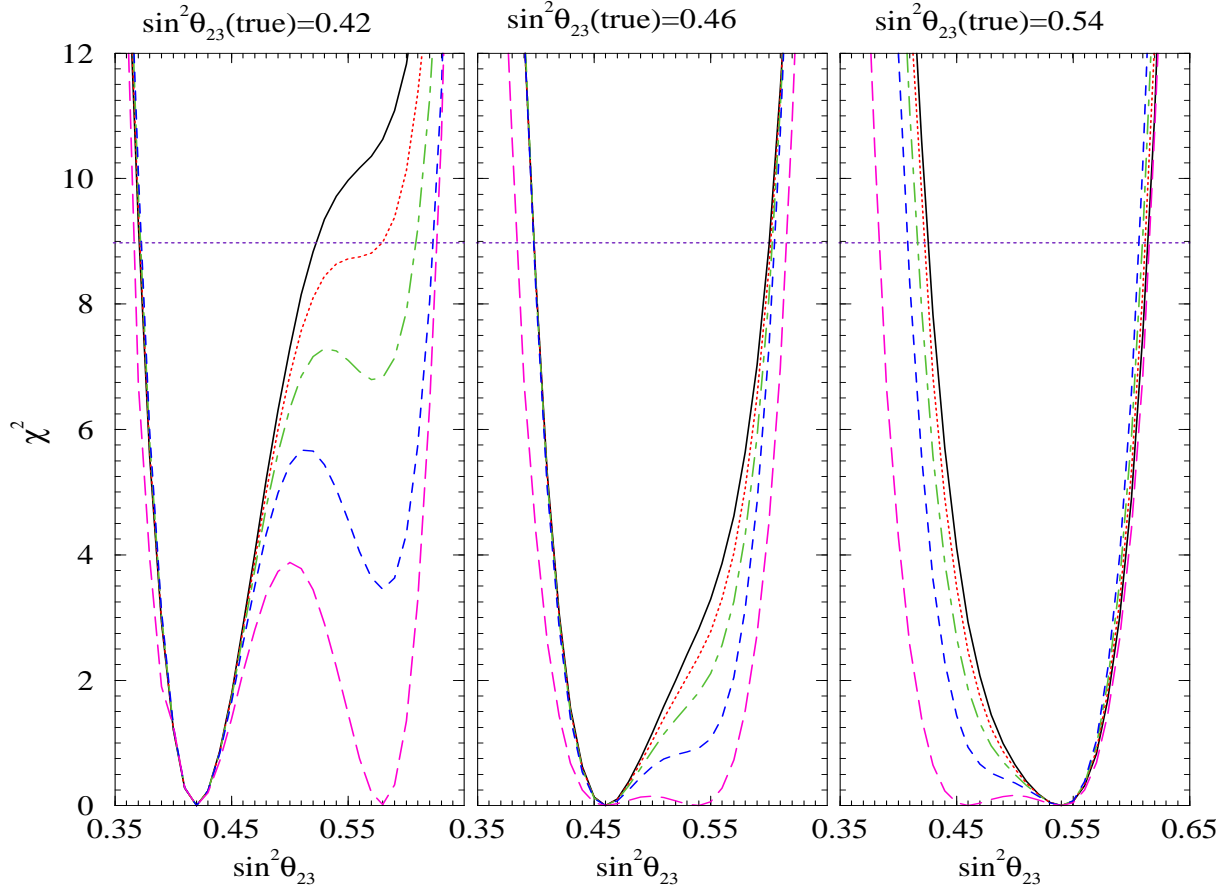


Figure 10:  $\chi^2$  as a function of  $\sin^2 \theta_{23}$ , showing the “octant sensitivity” of ICAL. The three panels project the expected sensitivity of ICAL for three different true value of  $\sin^2 \theta_{23}$ :  $\sin^2 \theta_{23}(\text{true}) = 0.42$  (left panel),  $\sin^2 \theta_{23}(\text{true}) = 0.46$  (middle panel) and  $\sin^2 \theta_{23}(\text{true}) = 0.54$  (right panel). The magenta long-dashed lines, blue short-dashed lines, green dot-dashed lines, red dotted lines and black solid lines are for  $\sin^2 \theta_{13}(\text{true}) = 0.00, 0.01, 0.02, 0.03$  and  $0.04$  respectively.

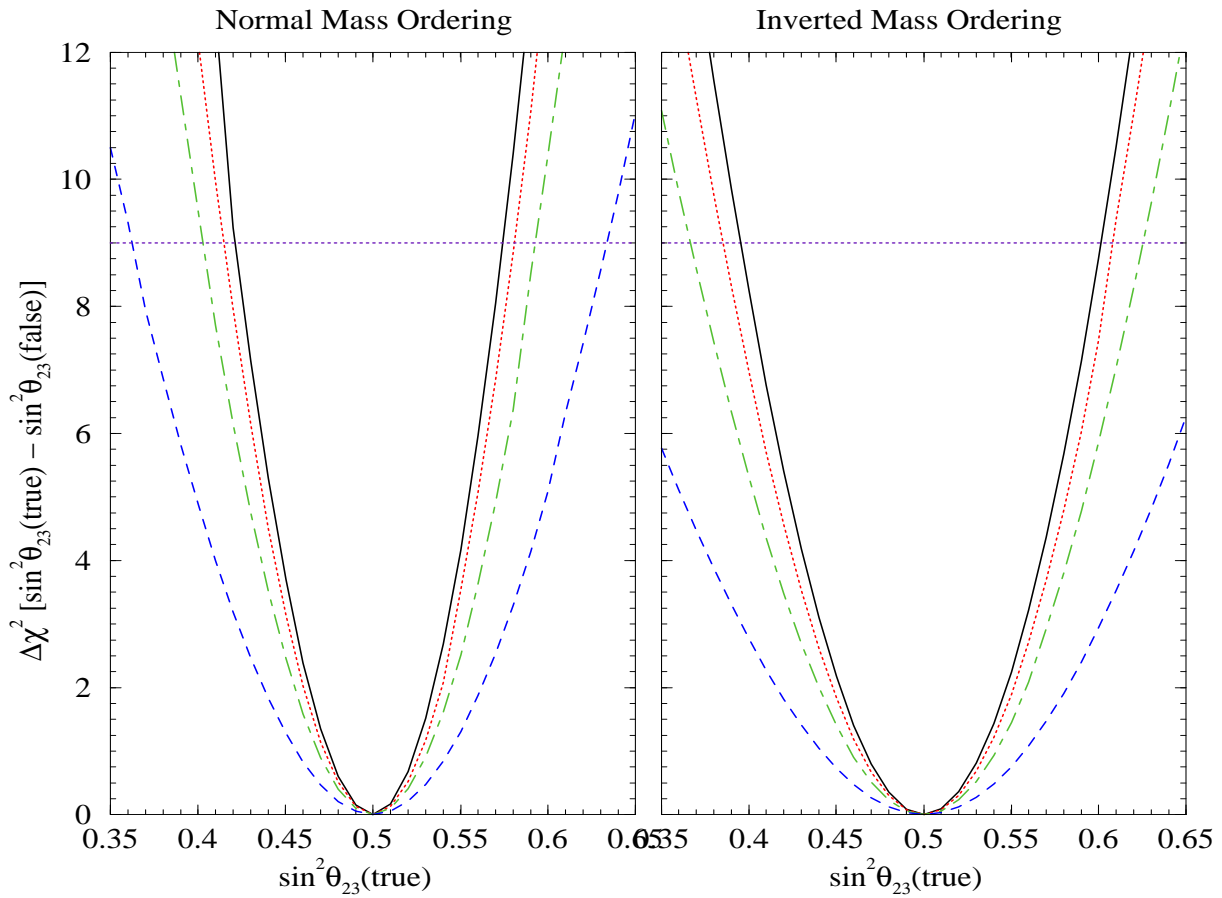


Figure 11:  $\Delta\chi^2$  as a function of  $\sin^2\theta_{23}(\text{true})$ , showing the octant sensitivity of ICAL for the normal (left panel) and inverted (right panel) neutrino mass ordering. The blue short-dashed lines, green dot-dashed lines, red dotted lines and black solid lines are for  $\sin^2\theta_{13}(\text{true}) = 0.01, 0.02, 0.03$  and  $0.04$  respectively.